

Determination of the neutron beta-decay asymmetry parameter A_0 using polarized
ultracold neutrons

DISSERTATION

A dissertation submitted in partial
fulfillment of the requirements for
the degree of Doctor of Philosophy
in Physics in the Department of
Physics and Astronomy at the
University of Kentucky

By
Michael A-P Brown
Lexington, Kentucky

Director: Dr. Bradley Plaster, Associate Professor of Physics
Lexington, Kentucky 2017

Copyright© Michael A-P Brown 2017

ABSTRACT OF DISSERTATION

Determination of the neutron beta-decay asymmetry parameter A_0 using polarized ultracold neutrons

The UCNA Experiment at the Los Alamos Neutron Science Center (LANSCE) is the first measurement of the β -decay asymmetry parameter A_0 using polarized ultracold neutrons (UCN). A_0 , which represents the parity-violating angular correlation between the direction of the initial neutron spin and the emitted decay electron's momentum, determines $\lambda = g_A/g_V$, the ratio of the weak axial-vector and vector coupling constants. A high-precision determination of λ is important for weak interaction physics, and when combined with the neutron lifetime it permits an extraction of the CKM matrix element V_{ud} solely from neutron decay. At LANSCE, UCN are produced in a pulsed, spallation driven solid deuterium source and then polarized via transport through a 7 T magnetic field. Their spins can then be flipped via transport through an Adiabatic Fast Passage spin flipper located in a low-field-gradient 1 T field region prior to transport to a decay storage volume situated within a 1 T solenoidal spectrometer. Electron detector packages located at each end provide for the measurement of decay electrons. Previous UCNA results (based on data collected in 2010 and earlier) were limited by systematic uncertainties, in particular those from the UCN polarization, calibration of the electron energy, and electron backscattering. This dissertation will present a background of Neutron Decay, an overview of the UCNA Experiment, followed by a detailed report on the entire analysis process for the 2011/2012 and 2012/2013 data sets.

KEYWORDS: UCN, Neutrons

Author's signature: Michael A-P Brown

Date: November 22, 2017

Determination of the neutron beta-decay asymmetry parameter A_0 using polarized
ultracold neutrons

By
Michael A-P Brown

Director of Dissertation: Dr. Bradley Plaster

Director of Graduate Studies: Dr. Chris Crawford

Date: November 22, 2017

ACKNOWLEDGMENTS

TABLE OF CONTENTS

| | |
|---|-----|
| Acknowledgments | iii |
| Table of Contents | iv |
| List of Figures | vi |
| List of Tables | ix |
| Chapter 1 Introduction to the theory of neutron β -decay | 1 |
| Chapter 2 UCNA Experiment | 2 |
| Chapter 3 UCNA Analysis | 3 |
| Chapter 4 UCNA Calibrations | 4 |
| Chapter 5 UCNA Results | 5 |
| 5.1 Constructing an Asymmetry | 5 |
| 5.1.1 Decay Rate Model | 5 |
| 5.1.2 Super-Ratio | 6 |
| 5.1.3 Extracting A_0 | 7 |
| 5.2 Systematic Corrections and Uncertainties | 8 |
| 5.2.1 Definition of Δ | 8 |
| 5.2.2 Energy Dependent Monte Carlo Corrections | 9 |
| 5.2.2.1 Backscattering Misidentification, Δ_2 | 9 |
| 5.2.2.2 Angular Acceptance, Δ_3 | 10 |
| 5.2.2.3 Uncertainty in Δ_{MC} | 15 |
| 5.2.2.4 Fidelity of Corrections | 18 |
| 5.2.3 Theory Modifications, Δ_{Th} | 20 |
| 5.2.3.1 Recoil Order Modification | 20 |
| 5.2.3.2 Radiative Modification | 22 |
| 5.2.4 Polarimetry Correction | 23 |
| 5.2.4.1 Extraction of A_0 using $\langle P \rangle_+$ and $\langle P \rangle_-$ | 23 |
| 5.2.5 Energy Reconstruction | 25 |
| 5.2.6 Background Contributions | 27 |
| 5.2.6.1 Background Subtraction | 28 |
| 5.2.6.2 Neutron Generated Backgrounds | 31 |
| 5.2.6.3 Veto Efficiency Uncertainty | 32 |
| 5.2.7 Miscellaneous Systematic Corrections and Uncertainties | 33 |
| 5.2.7.1 Wirechamber Efficiency | 33 |
| 5.2.7.2 Gain Uncertainty | 34 |

| | | | |
|---|---------|--|----|
| | 5.2.7.3 | Magnetic Field Nonuniformity | 35 |
| 5.3 | | Final Asymmetries | 36 |
| | 5.3.1 | Blinding | 37 |
| | 5.3.2 | Data Selection and Processing | 37 |
| | | 5.3.2.1 Cuts | 38 |
| | | 5.3.2.2 Data Taking Structure | 39 |
| | | 5.3.2.3 Analysis Choices | 39 |
| | 5.3.3 | Determining A_0 | 42 |
| | | 5.3.3.1 Combining Results | 42 |
| | | 5.3.3.2 Optimization of energy range | 42 |
| | | 5.3.3.3 Unblinded Result | 45 |
| 5.4 | | Future Outlook for UCNA and A_0 Measurements | 47 |
| Appendices | | | 51 |
| Chapter A Magnetic Field Non-Uniformity and the Super-Ratio | | | 51 |
| References | | | 53 |
| Vita | | | 56 |

LIST OF FIGURES

| | | |
|------|--|----|
| 5.1 | Backscattering corrections for analysis choice used in final asymmetry extraction (All event types included with 2/3 separated using the MWPC energy calibration) | 11 |
| 5.2 | Simulated detector efficiency as a function of electron energy for electrons which pass through the endcaps. | 12 |
| 5.3 | $\cos \theta$ corrections for analysis choice used in final asymmetry extraction (All event types included with 2/3 separated using the MWPC energy calibration) | 13 |
| 5.4 | Bin-by-bin Δ_2 corrections with polynomial fit shown in red. | 16 |
| 5.5 | Bin-by-bin Δ_3 corrections with polynomial fit shown in red. | 17 |
| 5.6 | Subfigures are broken into each event type. Left of each subfigure shows electron energy spectra for background subtracted data (blue open circles), Monte Carlo (black solid line), and the background (black closed circles). The right plot in each subfigure shows the fractional residual between background subtracted data and Monte Carlo, which is used when applying the conservative fractional uncertainty on the Monte Carlo corrections. | 19 |
| 5.7 | Extracted asymmetries from Monte Carlo data processed to mimic the experimental data. The dashed line indicates the 2017 PDG value $A_0 = -0.1184$ which was input into the simulation, thus the goal upon extraction of the final asymmetry parameter. The blue closed | 21 |
| 5.8 | Radiative and Recoil Order theory corrections to the measured asymmetry due to finite mass and non-zero charge of the final state proton. | 22 |
| 5.9 | Distributions of the residuals for each conversion electron source line used in the 2011-2012 calibration. The mean and sigma reported in the fit box are not the same as those used in the energy uncertainty. | 26 |
| 5.10 | Distributions of the residuals for each conversion electron source line used in the 2012-2013 calibration. The mean and sigma reported in the fit box are not the same as those used in the energy uncertainty. | 27 |
| 5.11 | Plot of energy uncertainty vs. reconstructed energy. The points plotted are the mean and σ of all reconstructed calibration peaks of Ce, Sn, and the lower and upper Bi peaks in that order. The x-axis offset in the 2011-2012 and 2012-2013 points is artificial and only meant for visualization. The bands represent the energy uncertainty at any given electron energy for the two data sets. | 28 |
| 5.12 | Plot of uncertainty on A_0 from the energy calibration vs. reconstructed energy for each of the 2011-2012 and 2012-2013 geometries. Weighting the energy dependent uncertainties shown here by the experimental statistics in each energy bin produces the final uncertainty on the extracted asymmetries. | 29 |

| | | |
|------|--|----|
| 5.13 | Total background spectra summed over all background runs for each event type in 2011-2012. | 29 |
| 5.14 | Total background spectra summed over all background runs for each event type in 2011-2012. | 30 |
| 5.15 | Integrated event rates for 2011-2012 East and West sides. The splitting in the β run rates is due to the difference between a spin-flipper “on” vs. spin-flipper “off” run, as the flipper “on” loading efficiency is approximately 2/3 that of a flipper “off” run. | 31 |
| 5.16 | Integrated event rates for 2012-2013 East and West sides. The splitting in the β run rates is due to the difference between a spin-flipper “on” vs. spin-flipper “off” run, as the flipper “on” loading efficiency is approximately 66% that of a flipper “off” run. | 32 |
| 5.17 | All raw super-ratio asymmetries as a function of group number, whether octet, quartet, or pair. There are no systematic corrections applied, and the asymmetries are integrated over the analysis window 190-740 keV. The split in the data is a batch of data from 2012-2013 that had to be discarded due to bad timing information. | 40 |
| 5.18 | Asymmetries for different subsets of data. The * signifies unseparated Type 2 and Type 3 events. The inset shows the asymmetries that include Type 0 events, as the uncertainties are too small to see in the main figure. The only corrections applied to these asymmetries are the energy dependent Monte Carlo corrections and the polarization correction. The error bars are purely statistical, so the observed agreement between asymmetries is a lower limit. | 41 |
| 5.19 | Plots of the fractional uncertainty on the extracted asymmetry for given minimum and maximum limits on the analysis window. The minimum of the combined systematic and statistical uncertainty is used for the final analysis window, $190 \text{ keV} < E_e < 740 \text{ keV}$ | 43 |
| 5.20 | Statistical and systematic errors used in minimization of the energy window. This is a projection of figure 5.19 about the minimum window cut of 190 keV to show the dependence on energy cut more effectively. | 44 |
| 5.21 | Ratio of the asymmetry for every possible energy window divided by the asymmetry of the window with the minimum uncertainty. The closer to the lower right hand corner, the larger the analysis window. We see that there is a region of highly consistent asymmetries covering the bottom right hand corner, which is where our analysis window of choice lies. When comparing to figure 5.19, we also see that, given the uncertainties for every analysis window, nearly all asymmetries are consistent within error. | 44 |
| 5.22 | Final beta decay spectrum from data (open circles), Monte Carlo (solid line), and the subtracted background (closed circles). The bottom shows the difference between the Monte Carlo spectrum and the data. | 45 |
| 5.23 | Final unblinded 2011-2012 and 2012-2013 asymmetry with all systematic corrections applied. The dashed line in a.) and c.) uses PDG $A_0 = -0.1184$ for comparison. The fits in b.) and d.) are over the final analysis window, $190 \text{ keV} < E_e < 740 \text{ keV}$. The uncertainties are statistical only. | 46 |

| | | |
|------|---|----|
| 5.24 | Status of V_{ud} , the neutron lifetime, and λ measurements. The λ result bands (vertical) are divided into pre-2002 [Bop+86; Yer+97; Lia+97] and post-2002 [Mos+01; Sch+08; Mun+13; Men+13] results, where the distinction is made using the date of the most recent result from each experiment. The right axis shows publication year for the individual lambda measurements included in the calculation of the λ bands (closed markers for post-2002, open markers for pre-2002). Note that the result of this work (Brown <i>et al.</i>) is the combined UCNA result from [Men+13] and the current analysis, and the Mund <i>et al.</i> result is the combined PERKEOII result from [Abe+02; Mun+13]. The diagonal bands are derived from neutron lifetime measurements and are separated into neutron beam [Yue+13; Byr+96] and UCN bottle experiments, which consist of material bottle storage [Ser+05; Arz+15; Ste+12; Pic+10; Mam+93] and magnetic bottle storage [PJ+17]. The V_{ud} band (horizontal) comes from superallowed $0^+ \rightarrow 0^+$ nuclear β -decay measurements [PG+16]. The error bands include scale factors as prescribed by the Particle Data Group [PG+16]. | 48 |
|------|---|----|

LIST OF TABLES

| | | |
|-----|--|----|
| 5.1 | Values for the effective statistical uncertainties from each event type. The value is reported as the uncertainty on $\frac{\Delta A}{A}$ | 18 |
| 5.2 | Values for the fractional uncertainties from each event type. The value is reported as the uncertainty on $\frac{\Delta A}{A}$ | 18 |
| 5.3 | Actual integrated event type fractions as percent of total events. Also reported is the % difference between Monte Carlo and data spectra for each event type. These are calculated over an energy window of 190-740, chosen to minimize total uncertainty as will be shown. | 20 |
| 5.4 | Results for average polarization fractions for each dataset in spin-flipper off (−) and spin-flipper on (+) states. | 23 |
| 5.5 | Mean and σ of each conversion electron residual distribution as used in the energy uncertainty, figure 5.11. | 25 |

Chapter 1

Introduction to the theory of neutron β -decay

Copyright© Michael A-P Brown, 2017.

Chapter 2

UCNA Experiment

Copyright© Michael A-P Brown, 2017.

Chapter 3

UCNA Analysis

Copyright© Michael A-P Brown, 2017.

Chapter 4

UCNA Calibrations

Copyright© Michael A-P Brown, 2017.

Chapter 5

UCNA Results

5.1 Constructing an Asymmetry

5.1.1 Decay Rate Model

Nominally the decay rate for polarized neutrons is expressed in terms of the spin vector and all possible correlations to the products [JTWJ57]. For simplicity, we begin by writing the differential decay rate only as a function of the electron asymmetry:

$$\Gamma(E, \Omega) = C \cdot S(E) \cdot (1 + A(E)\beta \cos \theta), \quad (5.1)$$

where $S(E)$ is the Standard Model differential decay rate for unpolarized β -decay, C is a constant which encompasses anything not included in $S(E)$ and serves the purpose of absorbing other constants, $A(E)$ is the energy dependent electron asymmetry parameter, $\beta \equiv v/c$ is the electron velocity, and θ is the angle between the spin of the neutron and the electron momentum.

We can also introduce an average polarization of the neutrons, giving

$$\Gamma(E, \Omega) = C \cdot S(E) \cdot \epsilon \cdot (1 + \langle P \rangle \cdot A(E)\beta \cos \theta), \quad (5.2)$$

where ϵ is the loading efficiency of neutrons in this spin state which I haven't absorbed into the constant for reasons to be seen, and $\langle P \rangle$ is the polarization, i.e. a number between 0 and 1 (very close to 1 in our case).

At this point, assumptions can be made regarding the experimental setup utilized to further express the decay rate in terms of detector rates. Due to the polarization being aligned with the 1 T magnetic field in the decay trap, electrons emitted with a momentum component along the spin will spiral towards one detector, while electrons with a component of momentum opposite the spin will be detected in the opposite

detector. If we fix the z-axis using the static position of our apparatus, we can call the detector at $\theta = 0$ detector 1 and the opposite detector 2.

Now, all electrons with $0 < \theta < \pi/2$ will head towards detector 1 and those with $\pi/2 < \theta < \pi$ will be directed towards detector 2. The solid angle can then be integrated out for each detector by integrating ϕ from $(0, 2\pi)$ and $\cos \theta$ over the intervals given, where the integral of $\cos \theta$ over detectors 1 and 2 yields $\pm 1/2$ respectively:

$$\Gamma_{1,2}(E) = 2\pi \cdot C \cdot S(E) \cdot \epsilon \cdot \eta_{1,2}(E) \left[1 + \langle P \rangle \cdot A(E) \beta \left(\pm_{1,2} \frac{1}{2} \right) \right], \quad (5.3)$$

$$\Gamma_{1,2}(E) = C' \cdot S(E) \cdot \epsilon \cdot \eta_{1,2}(E) \left[1 \pm_{1,2} \langle P \rangle \cdot A(E) \frac{\beta}{2} \right], \quad (5.4)$$

with $\eta_{1,2}(E)$ signifying energy dependent electron detection efficiencies for detectors 1 and 2.

Thus far we have assumed a fixed polarization, but in UCNA we have the ability to flip the spin of the neutrons prior to loading. We call these states flipper on (+) and flipper off (-), denoted by $\langle P \rangle_{\pm}$. The flipper on state introduces a negative in front of the polarization efficiency (due to the fact that $\vec{\sigma} \cdot \vec{p}_e$ is now negative for $0 < \theta < \pi/2$):

$$\Gamma_{1,2}^{\pm}(E) = C' \cdot S(E) \cdot \epsilon_{\pm} \cdot \eta_{1,2} \left[1 \pm_{1,2} (\mp \langle P \rangle_{\pm}) \cdot A(E) \frac{\beta}{2} \right], \quad (5.5)$$

where ϵ_{\pm} accounts for differing loading efficiencies for different spin states.

If we now assume that we are equally as efficient at polarizing in either spin state, we can say $\langle P \rangle_{+} = \langle P \rangle_{-} = \langle P \rangle$ (discussion for treatment of super-ratio not assuming this can be found in 5.2.4.1) giving:

$$\Gamma_{1,2}^{\pm}(E) = C' \cdot S(E) \cdot \epsilon_{\pm} \cdot \eta_{1,2} \left[1 \pm_{1,2} (\mp \langle P \rangle) \cdot A(E) \frac{\beta}{2} \right]. \quad (5.6)$$

5.1.2 Super-Ratio

A simple asymmetry over some energy bin for a single polarization state can be defined as

$$A_{\text{simple}} = \frac{\Gamma_1 - \Gamma_2}{\Gamma_1 + \Gamma_2}, \quad (5.7)$$

and assuming that the efficiencies η_1 and η_2 are the same one finds

$$A_{\text{simple}} = \langle P \rangle \cdot A(E) \cdot \frac{\beta}{2}, \quad (5.8)$$

where β is calculated as either the velocity associated with the energy at the center of the bin or the average energy of the bin.

In reality we cannot assume with certainty that the detectors are identical, but we can utilize the fact that we can flip the spins to cancel differing efficiencies. If we take two runs with opposite polarizations, we can define the super-ratio asymmetry in some energy range as:

$$A_{\text{SR}} = \frac{1 - \sqrt{R}}{1 + \sqrt{R}}, \quad (5.9)$$

where

$$R = \frac{\Gamma_1^+ \cdot \Gamma_2^-}{\Gamma_1^- \cdot \Gamma_2^+}. \quad (5.10)$$

Some algebra yields an identical expression to equation 5.8,

$$\begin{aligned} R &= \frac{[C'S(E)\epsilon_+\eta_1 [1 + (-\langle P \rangle) A(E)\frac{\beta}{2}]] [C'S(E)\epsilon_-\eta_2 [1 - (+\langle P \rangle) A(E)\frac{\beta}{2}]]}{[C'S(E)\epsilon_-\eta_1 [1 + (+\langle P \rangle) A(E)\frac{\beta}{2}]] [C'S(E)\epsilon_+\eta_2 [1 - (-\langle P \rangle) A(E)\frac{\beta}{2}]]}, \\ R &= \frac{[1 + (-\langle P \rangle) A(E)\frac{\beta}{2}] [1 - (+\langle P \rangle) A(E)\frac{\beta}{2}]}{[1 + (+\langle P \rangle) A(E)\frac{\beta}{2}] [1 - (-\langle P \rangle) A(E)\frac{\beta}{2}]}, \\ R &= \frac{[1 - \langle P \rangle A(E)\frac{\beta}{2}]^2}{[1 + \langle P \rangle A(E)\frac{\beta}{2}]^2}, \end{aligned}$$

and plugging into A_{SR}

$$\begin{aligned} A_{\text{SR}} &= \frac{1 - \frac{[1 - \langle P \rangle A(E)\frac{\beta}{2}]}{[1 + \langle P \rangle A(E)\frac{\beta}{2}]}}{1 + \frac{[1 - \langle P \rangle A(E)\frac{\beta}{2}]}{[1 + \langle P \rangle A(E)\frac{\beta}{2}]}}, \\ A_{\text{SR}} &= \frac{2\langle P \rangle A(E)\frac{\beta}{2}}{2}, \\ A_{\text{SR}} &= \langle P \rangle A(E)\frac{\beta}{2}. \end{aligned} \quad (5.11)$$

5.1.3 Extracting A_0

The quantity of interest is not the raw measured asymmetry, or even $A(E)$, but rather A_0 , which is also directly proportional to $\lambda = g_A/g_V$, yielding a direct measurement of the axial vector coupling constant if the CVC hypothesis is assumed.

A_0 manifests itself in our measured asymmetry as:

$$A_0 = A(E) \cdot (1 + \Delta(E)), \quad (5.12)$$

where $\Delta(E)$ is the energy dependent correction to the measured asymmetry from theory corrections and experimental systematic effects, all of which will be described in detail in 5.2.

Solving 5.2.4.1 for $A(E)$ and inserting into the above expression, we have

$$A_0 = \frac{(1 + \Delta(E)) \cdot A_{\text{SR}}(E)}{\langle P \rangle \cdot \beta/2}, \quad (5.13)$$

where again $\beta = v/c$.

With an energy dependent expression for A_0 , we can bin our data in discrete energy bins, evaluate β at the midpoint of the bin, apply appropriate energy dependent corrections, and then fit the resulting collection of A_0 values with a constant. Careful selection of the energy range to fit over is discussed in 5.3.3.2.

5.2 Systematic Corrections and Uncertainties

Measuring any quantity without imparting a systematic shift in the result due to imperfect experimental techniques is nearly impossible; but what is more dangerous to the result is not understanding these shifts. This section discusses how well we understand the theoretical and experimental effects present in the UCNA experiment that cause us to measure an asymmetry that is not directly equal to the parameter of interest, thus requiring corrections.

5.2.1 Definition of Δ

We adopt a similar formalism for systematic corrections as previously defined in [Men14], at least as far as the definition of the correction is concerned. If we have an asymmetry $A(E)$ measured without some correction i , then we can define $A'(E)$ as

$$A'(E) = (1 + \Delta_i(E)) \cdot A(E), \quad (5.14)$$

where $A'(E)$ is the new corrected asymmetry with systematic effect i removed. Rearrangement of the above equation provides a definition for Δ_i :

$$\Delta_i(E) = \frac{A'(E)}{A(E)} - 1 \quad (5.15)$$

This is useful as most corrections are determined by studying the effect on the asymmetry from some aspect of the experiment via Monte Carlo, so energy dependent corrections can be constructed and applied to data.

If the uncertainty on correction $\delta\Delta_i$ has been determined, we can also define the uncertainty on the resulting asymmetry $\delta A'(E)$ via normal error propagation techniques as

$$\delta A'(E) = A(E) \cdot \delta\Delta_i(E), \quad (5.16)$$

$$\frac{\delta A'(E)}{A'(E)} = \frac{\delta \Delta_i(E)}{1 + \Delta_i(E)}. \quad (5.17)$$

Now the collection of all corrections, if extracted independently, will commute, and thus provides

$$1 + \Delta(E) = (1 + \Delta_1(E))(1 + \Delta_2(E))(1 + \Delta_3(E)) \dots, \quad (5.18)$$

such that a final corrected asymmetry $A''' \dots$ can be written as

$$A''' \dots(E) = (1 + \Delta(E)) \cdot A(E),$$

$$A''' \dots(E) = \left(\prod_i (1 + \Delta_i(E)) \right) \cdot A(E). \quad (5.19)$$

The rest of this section is dedicated to determining all applicable Δ_i and their associated uncertainties.

5.2.2 Energy Dependent Monte Carlo Corrections

The Monte Carlo corrections rely solely on asymmetries from the simulated data with the entirety of the detector response model applied. For each individual data run, the conditions of the apparatus (calibration, pedestal, resolution, etc) are determined and a subset of the simulation data (roughly $16\times$ the data run) is processed using such conditions. This produces a higher statistics simulation of the individual runs, and therefore allows one to run the simulated octets through the asymmetry analysis in the exact same manner as the data. The fact that we know everything about each individual event in the simulation allows us to correct for effects to the asymmetries from the experimental conditions. Via equation 5.15, the asymmetry before and after a given correction can be used to determine the value of the correction to be applied to the data.

The Monte Carlo corrections are also further separated into corrections from misidentification of backscattering types, Δ_2 , and from angular acceptance effects, Δ_3 . In [UCNA2017], Δ_2 and Δ_3 correspond to $\Delta_{\text{backscattering}}$ and $\Delta_{\cos\theta}$ respectively.

5.2.2.1 Backscattering Misidentification, Δ_2

Imagine an event which initially heads towards the east detector, but it backscatters off of the decay trap window and never reaches a sensitive detector on the East side. The electron then heads towards the West detector where it is detected. Using only triggering information, this event would be improperly identified as a Type 0 event

with initial Western momentum. Experimental data possesses no way of properly identifying such events, so we rely on simulation. As mentioned previously, we have access to all initial conditions of each event, so upon forming an asymmetry one can properly identify all events which were detected as Type 0 and assure they are assigned to their proper initial direction. The comparison of the asymmetry before and after such a correction defines the Monte Carlo correction due to backscattering misidentification of Type 0 events. Let's call this $\Delta_{2,0}$, where the subscript 0 refers to the backscattering correction for Type 0 events. One can imagine that the same process can be repeated for each of the detected event types, giving us the following definition for the total Δ_2 correction:

$$1 + \Delta_2 = (1 + \Delta_{2,3})(1 + \Delta_{2,2})(1 + \Delta_{2,1})(1 + \Delta_{2,0}) \quad (5.20)$$

The corrections as a function of electron energy can be seen in figure 5.1. Application of the correction increases the magnitude of the measured asymmetry as it should, as missed backscattering events dilute the measured asymmetry. The uncertainties seen in the figure will be discussed in section 5.2.2.3. The leading contribution to the backscattering correction comes from Type 0 events, which are most likely to be misidentified and make up roughly 95% of the data. The other types trigger both detectors, so the odds of them being misidentified is much lower, although there is still appreciable correction to the Type 2 and Type 3 events due to the two types of events being closely related and the separation efficiency being only roughly 80%.

The difference between 2011-2012 and 2012-2013 corrections arises from the thinner decay trap windows in 2012-2013, which substantially reduces the $\Delta_{2,0}$ correction for misidentified Type 0 events. There is almost no effect on the other event types, as should be expected due to no dramatic change in event type fractions or triggering efficiencies for the two detector sides. Another way to think of this is that once an event passes through the endcap, it's likelihood of triggering the detector approaches 100% fairly quickly (see figure 5.2) and is not dependent on the changing geometry, so the corrections for backscattering events are robust. Differing window thicknesses do however modify the number of misidentified Type 0 events, decreasing them in the case of thinner windows as more electrons should pass through without scattering, thus decreasing the magnitude of the $\Delta_{2,0}$ correction by definition.

5.2.2.2 Angular Acceptance, Δ_3

Remember from equation 5.1 that the decay rate depends on $\beta \cos \theta$ and that we proceeded to integrate over one hemisphere of the detector giving $\langle \cos \theta \rangle = 1/2$. We

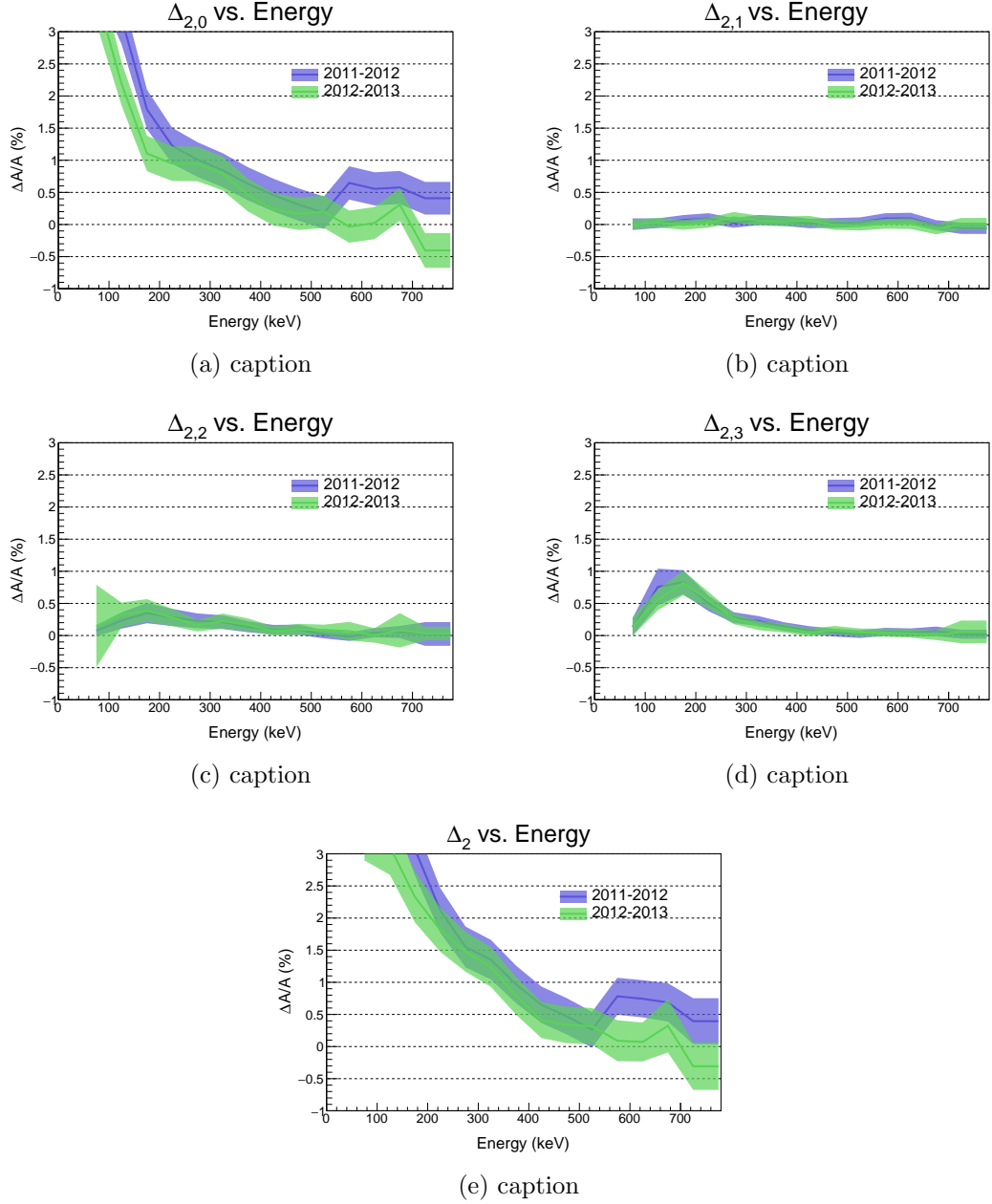


Figure 5.1: Backscattering corrections for analysis choice used in final asymmetry extraction (All event types included with 2/3 separated using the MWPC energy calibration)

also use the midpoint of the energy bin of interest when evaluating $\beta = v/c$, which isn't equal to the average value in a single bin due to the non-constant shape of the electron energy spectrum. What is described is an approximation of the form $\langle \beta \cos \theta \rangle \approx \beta_{\text{mid}}/2$. The actual value of $\langle \beta \cos \theta \rangle$ must be determined using simulated data, as events are lost in an energy and angle dependent manner, with lower energy

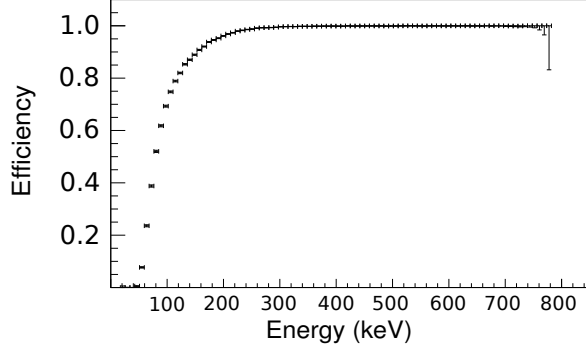


Figure 5.2: Simulated detector efficiency as a function of electron energy for electrons which pass through the endcaps.

and high pitch angle events being most likely to be lost. Δ_3 attempts to remove this angular dependence on event acceptance while also correcting for the slight systematic effect of approximating β at the midpoint.

If we define the asymmetry which properly accounts for the true $\langle \beta \cos \theta \rangle$ as A' and the asymmetry which uses our approximation $\langle \beta \cos \theta \rangle \approx \beta_{\text{mid}}/2$ as A , then we see from 5.2.4.1 that

$$A' = \frac{A_{\text{SR}}}{\langle \beta \cos \theta \rangle \langle P \rangle} \quad (5.21)$$

and

$$A = \frac{A_{\text{SR}}}{\frac{\beta}{2} \langle P \rangle}. \quad (5.22)$$

Then from our generic definition for a systematic correction, equation 5.15, we have

$$\Delta_3(E) = \frac{A'}{A} - 1$$

and upon use of equations 5.21 and 5.22,

$$\Delta_3(E) = \frac{\frac{\beta}{2}}{\langle \beta \cos \theta \rangle} - 1. \quad (5.23)$$

From this, we see that it is sufficient to determine $\langle \beta \cos \theta \rangle$ from simulation and calculate the energy dependent corrections.

In previous analyses, this correction was done for the event population as a whole, producing only a single correction Δ_3 . New work in defining this correction allows for separation of the correction into individual contributions from each event type,

$$1 + \Delta_3 = (1 + \Delta_{3,3})(1 + \Delta_{3,2})(1 + \Delta_{3,1})(1 + \Delta_{3,0}). \quad (5.24)$$

This is more difficult than separating Δ_2 , as it requires more than a simple event-by-event reassignment to the proper initial direction. This requires evaluation of an

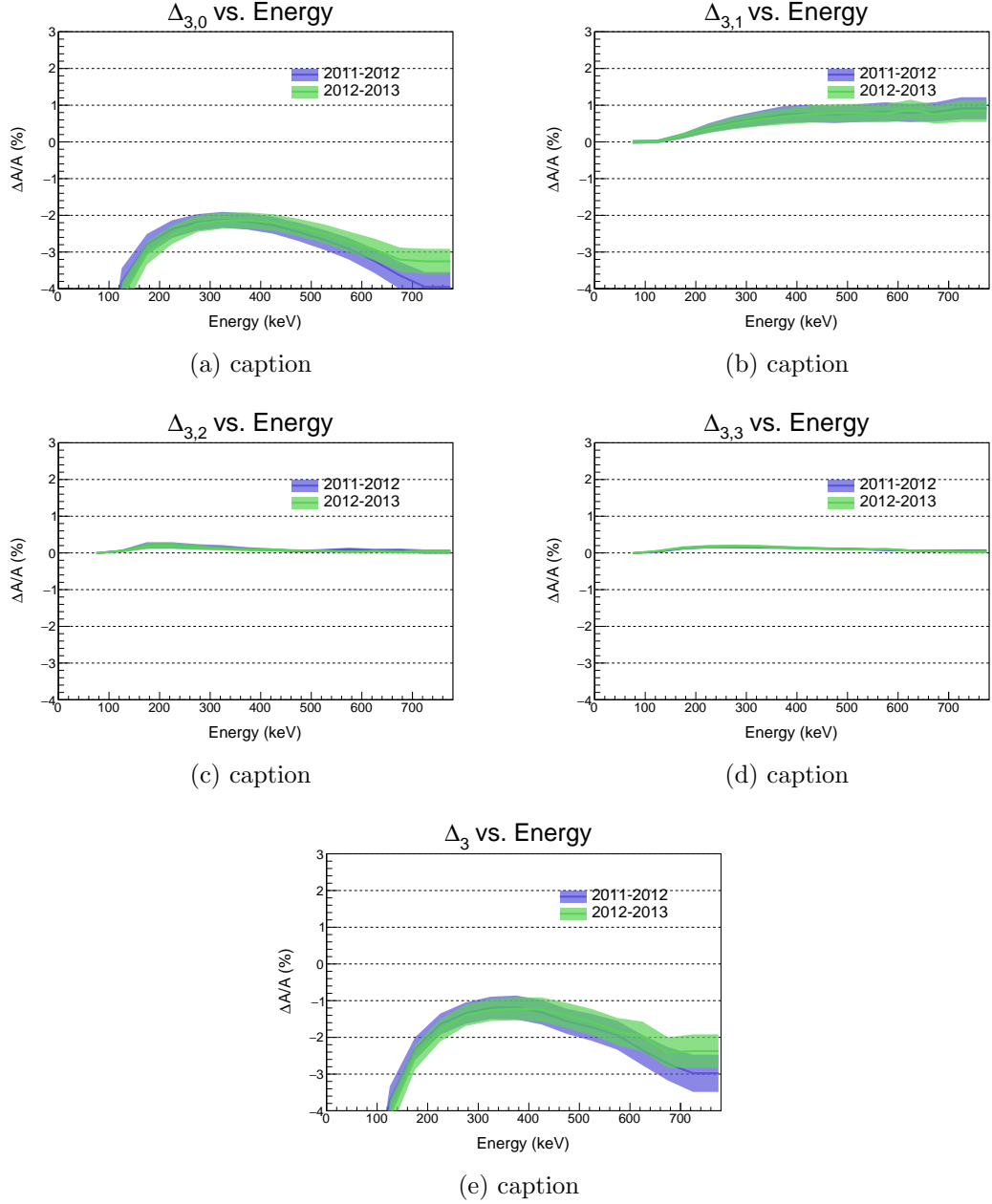


Figure 5.3: $\cos \theta$ corrections for analysis choice used in final asymmetry extraction (All event types included with 2/3 separated using the MWPC energy calibration)

average observable in the simulation, so we need a way to realize the contribution of each event type to the average. The key is to use the individual asymmetry of each event type and its respective angular correction, and then define the total correction as a function of the individual corrections.

Determination of the $\Delta_{3,i}$ corrections starts with a new definition of the uncor-

rected combined asymmetry¹ involving the individual asymmetries of each event type. The following definitions will be useful in this derivation.

$$\begin{aligned}
A &\equiv \text{Uncorrected total asymmetry} \\
A^i &\equiv \text{Asymmetry for event type } i \\
f^i &\equiv \text{Statistical weight for event type } i \\
\Delta_3^i &\equiv \text{Angle correction to } A^i \text{ for event type } i \\
A^{\text{corr},i} &\equiv \text{Corrected asymmetry for event type } i \\
A_{\text{corr},i} &\equiv \text{Total asymmetry corrected for event type } i \\
\Delta_{3,i} &\equiv \text{Angle correction to total asymmetry } A \text{ for event type } i
\end{aligned}$$

Now we can define the uncorrected total asymmetry as

$$A = \sum_i f^i A^i \quad (5.25)$$

where the sum runs over the event types that are to be included in the determination of the asymmetry. As will be seen in 5.3.2.3, one can include any combination of event types to produce many different asymmetries, so this definition allows for use across any choice of event types.

Next we can define Δ_3^i , or the angle correction to the asymmetry when only including type i events, using equation 5.23 and only including type i events when calculating $\langle \beta \cos \theta \rangle$. Then we can write down an expression for the corrected asymmetry for that event type as

$$A^{\text{corr},i} = (1 + \Delta_3^i) A^i. \quad (5.26)$$

It then follows that the total asymmetry corrected for the same event type i becomes

$$A_{\text{corr},i} = A^{\text{corr},i} + \sum_{j \neq i} f^j A^j. \quad (5.27)$$

With these relationships at hand, it is straightforward to follow the prescription to write down an expression for $\Delta_{3,i}$ in terms of known values:

$$\begin{aligned}
\Delta_{3,i} &= \frac{A_{\text{corr},i}}{A} - 1 = \frac{A_{\text{corr},i} - A}{A} = \frac{f^i (A^{\text{corr},i} - A^i)}{A} \\
&\Rightarrow \Delta_{3,i} = \frac{f^i A^i}{A} \Delta_3^i.
\end{aligned} \quad (5.28)$$

¹This definition of the asymmetry is only used for analysis of this correction, and not for extraction of the final asymmetry.

The energy dependent $\Delta_{3,i}$ corrections are shown in figure 5.3. The impact of applying the combined Δ_3 correction is to decrease the magnitude of the measured asymmetry. This comes from the dominance of the $\Delta_{3,0}$ portion, or the correction due to the acceptance of Type 0 events. Type 0 events are more likely lost when they are high pitch angle, low energy events. Such events carry little asymmetry information ($\beta \cos \theta$ gets small) as seen in equation 5.1. Measurement of an asymmetry which has these low-asymmetry events removed yields a higher than expected asymmetry, thus necessitating a correction which decreases the magnitude of the measured asymmetry. The contribution of the backscattering events to the angular correction have the opposite sign and act to increase the magnitude of the measured asymmetry. While this may seem counterintuitive due to the detectors nominally preferentially selecting low pitch angle, high energy events, this sign is due to the backscattering events being overwhelmingly high pitch angle events. Therefore $|\langle \cos \theta \rangle|$ over one hemisphere of the decay trap will be less than the nominal value $1/2$ for all backscattering events types, calling for a correction which increases the magnitude of the measured asymmetry.

5.2.2.3 Uncertainty in Δ_{MC}

In the analysis of the previous 2010 data set [Men+13] a conservative 25% uncertainty was applied to all Monte Carlo corrections, where the 25% came from the observed discrepancy between data and Monte Carlo backscattering fractions. The issue with such a correction is obvious when the correction itself is zero, as any percent uncertainty on that correction would also be zero. One might argue that the absence of a correction would imply the absence of an uncertainty in that correction, but we must remember that the corrections are determined using Monte Carlo simulations of finite statistics, thus even a 0% correction comes with an uncertainty. Another concern is that not all event type fractions disagree with Monte Carlo by 25%, and the backscattering spectra that do disagree contribute little statistically to the asymmetry. Also, the asymmetry is no longer dominated by statistical uncertainty, and, as will be seen in section 5.2.5, the uncertainty due to energy reconstruction has been reduced, thus the ultra conservative worst-case scenario may artificially limit our result. With these concerns taken into consideration, a new method was developed to assess the uncertainty on the Monte Carlo corrections motivated by the fractional discrepancies between data and simulation for each event type, denoted by $\delta_{\text{frac}}\Delta_{i,j}$, and the statistical fluctuations in the corrections themselves, $\delta_{\text{stat}}\Delta_{i,j}$.

We further break up the statistical uncertainty into two parts and add these in quadrature to get $\delta_{\text{stat}}\Delta_{i,j}$. There is an obvious uncertainty that comes from simply

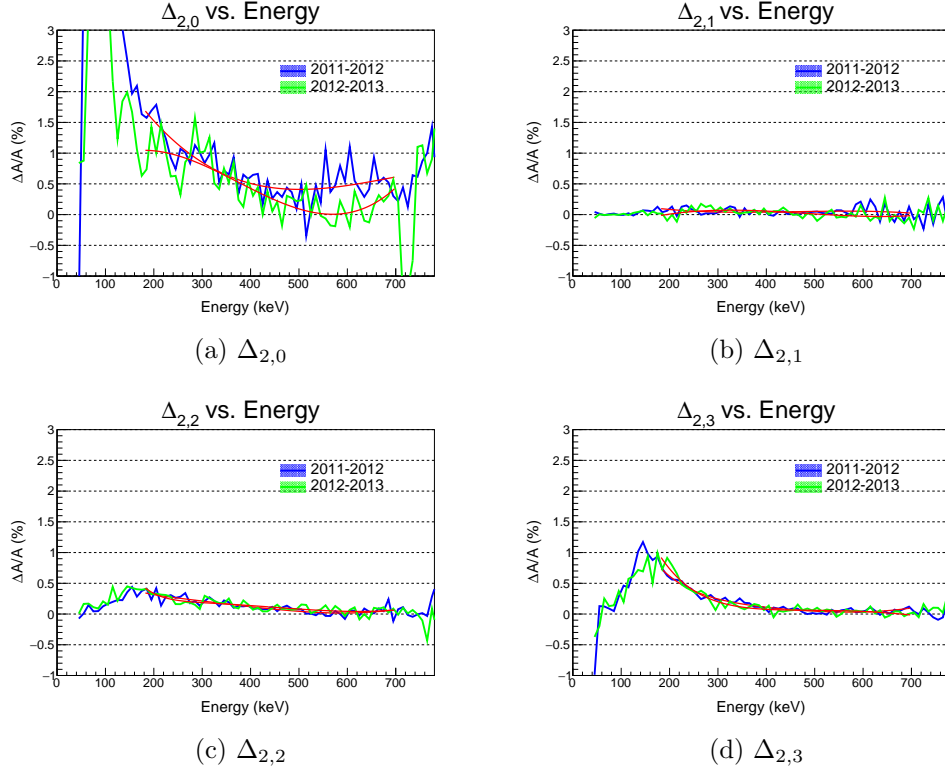


Figure 5.4: Bin-by-bin Δ_2 corrections with polynomial fit shown in red.

propagating the statistics of the simulation through the correction, which we will call $\delta_{\text{stat}}^{\text{pure}} \Delta_{i,j}$. This uncertainty doesn't seem to account for the fluctuations we see in the correction though, as seen in figure 5.4 a.) where the correction, when plotted for each energy bin, oscillates at the roughly 0.25% correction level at higher energies. This oscillation may be due to correlations between the Monte Carlo events used to simulate each run, as there are only 200 million events for each geometry and the events are chosen randomly from this pool of events, or it could be from improper sampling of the decay phase space for unknown reasons when generating the Monte Carlo events. Either way, we account for this observed statistical fluctuation using what we call the effective statistical uncertainty, or $\delta_{\text{stat}}^{\text{eff}} \Delta_{i,j}$, which gives us

$$\delta \Delta_{i,j} = \sqrt{(\delta_{\text{frac}} \Delta_{i,j})^2 + (\delta_{\text{stat}}^{\text{pure}} \Delta_{i,j})^2}$$

$$\delta \Delta_{i,j} = \sqrt{(\delta_{\text{frac}} \Delta_{i,j})^2 + (\delta_{\text{stat}}^{\text{pure}} \Delta_{i,j})^2 + (\delta_{\text{stat}}^{\text{eff}} \Delta_{i,j})^2}. \quad (5.29)$$

To determine the effective statistical uncertainty $\delta_{\text{stat}}^{\text{eff}} \Delta_{i,j}$, we begin by fitting the bin-by-bin Monte Carlo corrections with a combination of a decaying exponential and

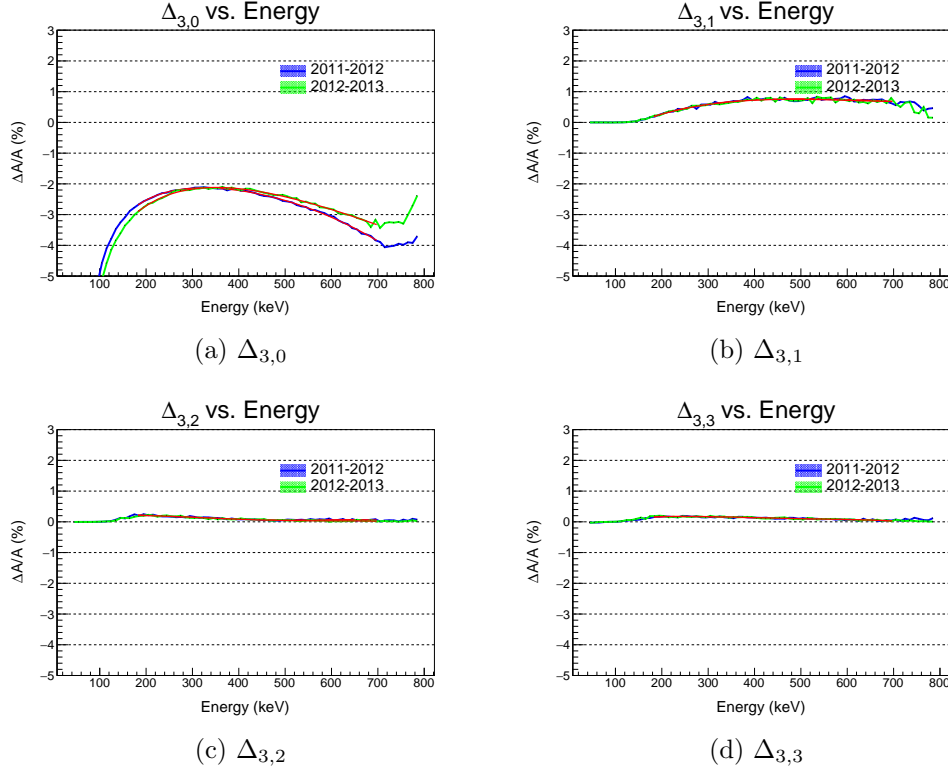


Figure 5.5: Bin-by-bin Δ_3 corrections with polynomial fit shown in red.

a third-order polynomial,

$$f(E) = C_0 e^{-C_1 E} + C_2 + C_3 E + C_4 E^2 + C_5 E^3. \quad (5.30)$$

Then one can form residuals for every energy bin by subtracting the actual value of the correction from the value given by the fit. The RMS of the residuals was then calculated separately for each $\Delta_{i,j}$ and each geometry. The effective statistical uncertainty was set to the larger RMS from the two geometries for each $\Delta_{i,j}$ to be conservative. The values for $\delta_{\text{stat}}^{\text{eff}} \Delta_{i,j}$ can be found in table 5.1.

Assigning values for the fractional uncertainties on each correction is more straightforward and comes from looking at the spectral discrepancies of each event type. We have a Monte Carlo predicted spectrum and a data spectrum for each of our event types, so we can construct a fractional residual between these spectra as seen in figure 5.6 simply using $\frac{\text{MC}}{\text{Data}} - 1$. Then by choosing approximately the maximum fractional residual over energies of interest (180-700 keV, starting at roughly the lower limit on our analysis energy window and ending when the statistics drop below 10% of the maximum rate), we conservatively set the fractional discrepancy of our corrections. The values of $\delta_{\text{frac}} \Delta_{i,j}$ are tabulated in table 5.2. One should note that the integrated

Table 5.1: Values for the effective statistical uncertainties from each event type. The value is reported as the uncertainty on $\frac{\Delta A}{A}$.

| | % Uncert. |
|--|-------------|
| $\delta_{\text{stat}}^{\text{eff}} \Delta_{2,0}$ | ± 0.25 |
| $\delta_{\text{stat}}^{\text{eff}} \Delta_{2,1}$ | ± 0.074 |
| $\delta_{\text{stat}}^{\text{eff}} \Delta_{2,2}$ | ± 0.062 |
| $\delta_{\text{stat}}^{\text{eff}} \Delta_{2,3}$ | ± 0.059 |
| $\delta_{\text{stat}}^{\text{eff}} \Delta_{3,0}$ | ± 0.04 |
| $\delta_{\text{stat}}^{\text{eff}} \Delta_{3,1}$ | ± 0.04 |
| $\delta_{\text{stat}}^{\text{eff}} \Delta_{3,2}$ | ± 0.02 |
| $\delta_{\text{stat}}^{\text{eff}} \Delta_{3,3}$ | ± 0.02 |

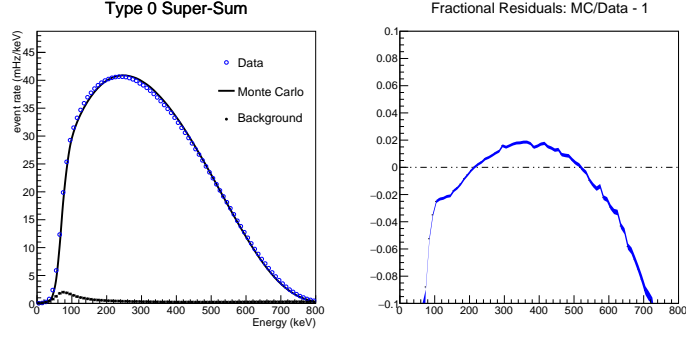
Table 5.2: Values for the fractional uncertainties from each event type. The value is reported as the uncertainty on $\frac{\Delta A}{A}$.

| | % Uncert. |
|-------------------------------------|------------|
| $\delta_{\text{frac}} \Delta_{2,0}$ | ± 0.10 |
| $\delta_{\text{frac}} \Delta_{2,1}$ | ± 0.30 |
| $\delta_{\text{frac}} \Delta_{2,2}$ | ± 0.40 |
| $\delta_{\text{frac}} \Delta_{2,3}$ | ± 0.20 |
| $\delta_{\text{frac}} \Delta_{3,0}$ | ± 0.10 |
| $\delta_{\text{frac}} \Delta_{3,1}$ | ± 0.30 |
| $\delta_{\text{frac}} \Delta_{3,2}$ | ± 0.40 |
| $\delta_{\text{frac}} \Delta_{3,3}$ | ± 0.20 |

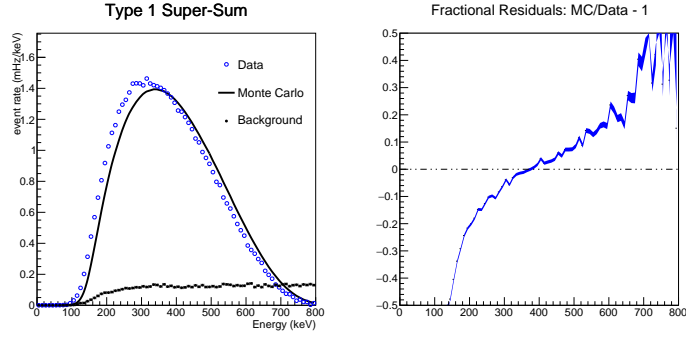
agreement between Monte Carlo and data is much better than these conservative fractional uncertainties, as seen in table 5.3.

5.2.2.4 Fidelity of Corrections

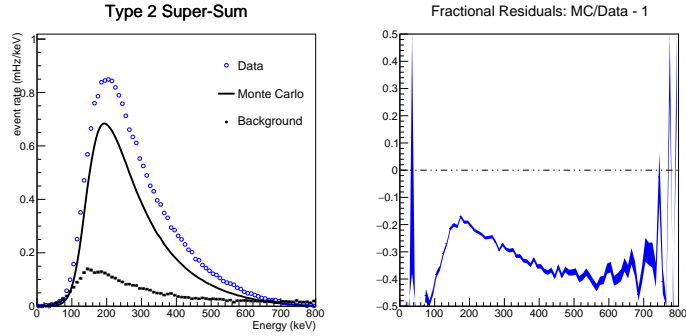
As mentioned in section ??, an asymmetry equal to the 2017 PDG value ($A_0 = -0.1184$) was incorporated into the Monte Carlo event generator, along with all radiative and recoil order effects. This allows us to extract the Monte Carlo corrections from event distributions which mimic our measurement populations, but it also allows us to apply our corrections to the Monte Carlo rates to see what we extract for A_0 . Because we process the simulations such that we have complementary simulated



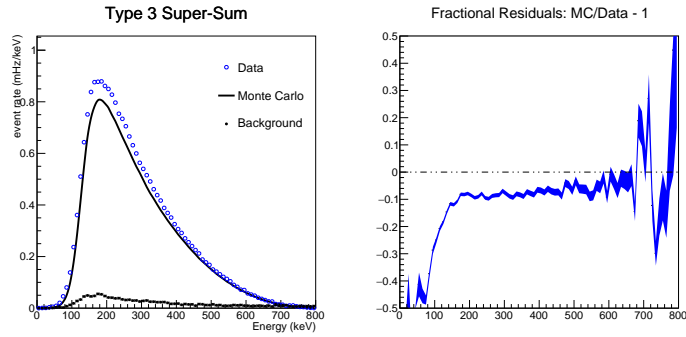
(a) Type 0



(b) Type 1



(c) Type 2



(d) Type 3

Figure 5.6: Subfigures are broken into each event type. Left of each subfigure shows electron energy spectra for background subtracted data (blue open circles), Monte Carlo (black solid line), and the background (black closed circles). The right plot in each subfigure shows the fractional residual between background subtracted data and Monte Carlo, which is used when applying the conservative fractional uncertainty on the Monte Carlo corrections.

Table 5.3: Actual integrated event type fractions as percent of total events. Also reported is the % difference between Monte Carlo and data spectra for each event type. These are calculated over an energy window of 190-740, chosen to minimize total uncertainty as will be shown.

| | Type 0 | Type 1 | Type 2 | Type 3 |
|---------|--------|--------|--------|--------|
| Data | 94.44 | 3.31 | 1.09 | 1.15 |
| MC | 94.86 | 3.30 | 0.78 | 1.06 |
| % Diff. | 0.44 | -0.29 | -28.24 | -7.91 |

data for every β -decay run (with the Monte Carlo having $\approx 16 \times$ data statistics), we can run the simulated data through the same asymmetry extraction method and compare the extracted fully-corrected asymmetry to the PDG input value. Figure 5.7 shows the Monte Carlo corrected asymmetries for all analysis choices. The agreement across all event types indicates the energy dependent Monte Carlo corrections are self-consistent.

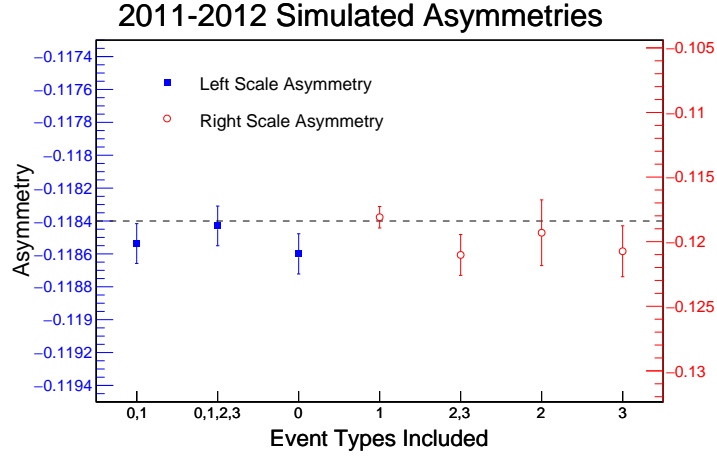
5.2.3 Theory Modifications, Δ_{Th}

The β -decay asymmetry parameter of interest, A_0 , assumes an infinitely massive, neutral proton in the final state and electrons that, once emitted in the decay, can be detected with precisely their emission energy and direction. This is not the practical scenario though, as the proton has charge and finite mass, and the electron is immersed in the coulomb field of the proton. Taking such non-ideal conditions into consideration means relying on theoretical modifications to the asymmetry we measure in order to extract A_0 .

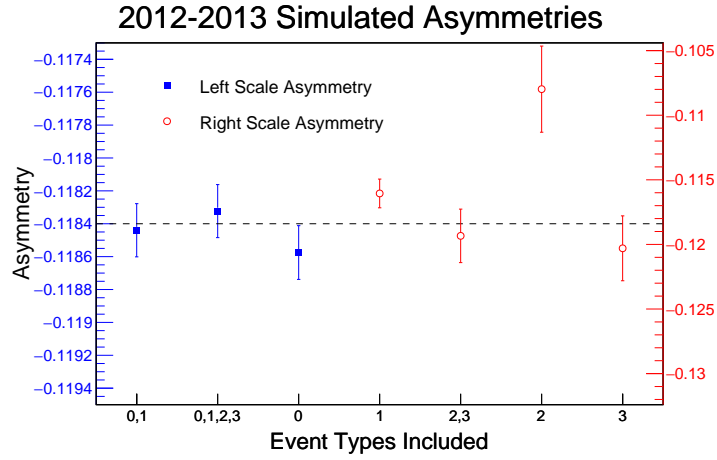
The theoretical effects come in two flavors: recoil-order modifications to address the finite mass of the final state proton and radiative corrections to remove effects from the electron interacting with the field of the proton. The energy dependence of each can be seen in 5.8.

5.2.3.1 Recoil Order Modification

The recoil order and weak magnetism modification applied are those from Bilen'kiĭ *et al.* [Bil+60] and further upheld by Wilkinson [Wil82]. The correction takes the



(a) 2011-2012



(b) 2012-2013

Figure 5.7: Extracted asymmetries from Monte Carlo data processed to mimic the experimental data. The dashed line indicates the 2017 PDG value $A_0 = -0.1184$ which was input into the simulation, thus the goal upon extraction of the final asymmetry parameter. The blue closed

form

$$A(E) = A_0 \left(1 + \frac{\lambda + \mu}{\lambda(1 - \lambda)(1 + 3\lambda^2)} \frac{1}{M} \left(\lambda^2 + \frac{2}{3}\lambda - \frac{1}{3} \right) E_0 - \left(\lambda^3 + 3\lambda^2 + \frac{5}{3}\lambda - \frac{1}{3} \right) E + \left(2\lambda^2(1 - \lambda) \right) \frac{1}{E} \right), \quad (5.31)$$

where E is the electron kinetic energy, E_0 is the endpoint energy of the electron, $\lambda \equiv \frac{g_A}{g_V}$, and $\mu \equiv \mu_p - \mu_n$. The correction is reported at the 0.001% level on λ , or roughly 0.004% on A_0 [Wil82].

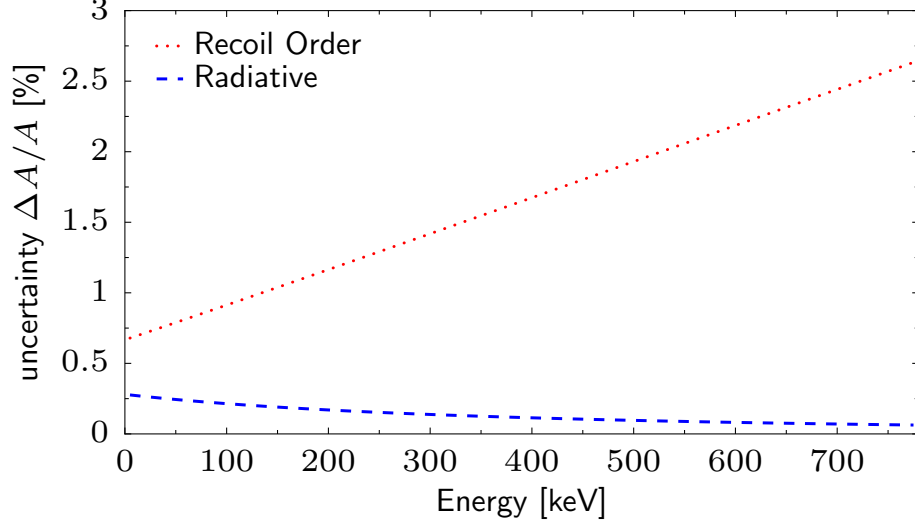


Figure 5.8: Radiative and Recoil Order theory corrections to the measured asymmetry due to finite mass and non-zero charge of the final state proton.

The correction to the asymmetry, when integrated over the analysis window and weighted by statistics, is $-1.68(3)\%$ and $-1.67(3)\%$ for 2011-2012 and 2012-2013 respectively. The uncertainties are conservative and carried over from the previous analysis.

It should be noted that the formalism above includes only the usual vector and axial vector terms in the hadronic current. Other work from Gardner and Zhang [GZ01] includes all potential interaction terms, including BSM couplings. The results agree with those from Wilkinson when the BSM terms are neglected.

5.2.3.2 Radiative Modification

Sirlin first calculated the $O(\alpha)$ corrections to the unpolarized neutron β -decay electron energy spectrum [Sir67], followed a few years later by Shann's extension of the formalism for polarized neutrons. The asymmetry is modified by the amount $\frac{\alpha}{2\pi}(h - g)$, where

$$h - g = 4 \left(\frac{E_0 - E}{3E\beta^2} \right) \left(\frac{\tanh^{-1} \beta}{\beta} - 1 \right) \left(1 - \beta^2 + \frac{E_0 - E}{8E} \right) + \frac{\tanh^{-1} \beta}{\beta} \left(2 - 2\beta^2 - \frac{(E - E_0)^2}{6E^2} \right), \quad (5.32)$$

E and E_0 are the electron energy and endpoint energy, and $\beta \equiv v/c$. The correction over the analysis energy window is $-0.12(5)\%$ for both 2011-2012 and 2012-2013.

5.2.4 Polarimetry Correction

As mentioned in section ??, an equilibrium population of neutron spins develops within the decay trap during a β -decay run. While this population is dominated by the spin-state of choice ($> 99\%$), precise determination of the average polarization is important as it directly affects the final extracted asymmetry as shown in equation 5.13. The determination of the polarization values were carried out in a separate analysis by Eric Dees of North Carolina State University. The values for the \pm spin-flipper states for each geometry are given in table 5.4.

Table 5.4: Results for average polarization fractions for each dataset in spin-flipper off ($-$) and spin-flipper on ($+$) states.

| 2011-2012 | | 2012-2013 | |
|-----------------------|-----------------------|-----------------------|-----------------------|
| $\langle P \rangle_-$ | $\langle P \rangle_+$ | $\langle P \rangle_-$ | $\langle P \rangle_+$ |
| 0.9970(30) | 0.9939(25) | 0.9979(15) | 0.9952(20) |

There are two options for applying a polarization correction, namely calculate an average polarization $\langle P \rangle$ which is averaged over both spin states and simply divide this out of the measured asymmetry as shown in equation 5.13, or utilize the separate $\langle P \rangle_{\pm}$ values. The second method is not a simple division of either term but rather a more complicated combination due to the usage of the super-ratio. This second method was adopted for this analysis and is described below.

5.2.4.1 Extraction of A_0 using $\langle P \rangle_+$ and $\langle P \rangle_-$

Using each of the $\langle P \rangle_{\pm}$ values requires modification of our initial asymmetry formalism from 5.1 [You17]. We can no longer make the assumption that $\langle P \rangle_+ = \langle P \rangle_-$ if we want to treat them separately. Let us start our new derivation from equation 5.6, which now becomes

$$\Gamma_{1,2}^{\pm}(E) = C' \cdot S(E) \cdot \epsilon_{\pm} \cdot \eta_{1,2} \left[1 \pm_{1,2} (\mp \langle P \rangle_{\pm}) \cdot A(E) \frac{\beta}{2} \right] \quad (5.33)$$

under the substitution $\langle P \rangle \rightarrow \langle P \rangle_{\pm}$.

The super-ratio now must be written as

$$R = \frac{\Gamma_1^+ \cdot \Gamma_2^-}{\Gamma_1^- \cdot \Gamma_2^+} = \frac{[1 + (-\langle P \rangle_+) A(E) \frac{\beta}{2}] [1 - (+\langle P \rangle_-) A(E) \frac{\beta}{2}]}{[1 + (+\langle P \rangle_-) A(E) \frac{\beta}{2}] [1 - (-\langle P \rangle_+) A(E) \frac{\beta}{2}]},$$

and upon letting $\xi = A(E)\frac{\beta}{2}$ we have

$$R = \frac{(1 - \xi\langle P \rangle_+)(1 - \xi\langle P \rangle_-)}{(1 + \xi\langle P \rangle_-)(1 + \xi\langle P \rangle_+)}. \quad (5.34)$$

We are interested in solving for $A(E)$, or ξ , so we can rearrange 5.34 to give

$$\begin{aligned} R(1 + \xi\langle P \rangle_-)(1 + \xi\langle P \rangle_+) &= (1 - \xi\langle P \rangle_+)(1 - \xi\langle P \rangle_-), \\ R\left(1 + \xi(\langle P \rangle_- + \langle P \rangle_+) + \xi^2\langle P \rangle_- \langle P \rangle_+\right) &= \left(1 - \xi(\langle P \rangle_- + \langle P \rangle_+) + \xi^2\langle P \rangle_- \langle P \rangle_+\right), \\ 0 &= \xi^2\langle P \rangle_- \langle P \rangle_+ (1 - R) - \xi(\langle P \rangle_- + \langle P \rangle_+) (1 + R) + (1 - R), \end{aligned}$$

and

$$0 = \xi^2\langle P \rangle_- \langle P \rangle_+ - \xi(\langle P \rangle_- + \langle P \rangle_+) \left(\frac{1+R}{1-R}\right) + 1, \quad (5.35)$$

which has roots (let $\gamma = \frac{1+R}{1-R}$)

$$\xi = \frac{\gamma(\langle P \rangle_- + \langle P \rangle_+) \pm \sqrt{\gamma^2(\langle P \rangle_- + \langle P \rangle_+)^2 - 4\langle P \rangle_- \langle P \rangle_+}}{2\langle P \rangle_- \langle P \rangle_+}. \quad (5.36)$$

To choose the proper root, we set $\langle P \rangle_- = \langle P \rangle_+ = \langle P \rangle$ and determine which root returns the original expression for the super-ratio as given in equations 5.9 and 5.2.4.1, namely

$$A_{\text{SR}} = \frac{1 - \sqrt{R}}{1 + \sqrt{R}} = \langle P \rangle A(E) \frac{\beta}{2}.$$

Upon doing so, we find that the negative root is the correct solution, which results in a new expression for $A(E)$ of

$$A(E) = \frac{\gamma(\langle P \rangle_- + \langle P \rangle_+) - \sqrt{\gamma^2(\langle P \rangle_- + \langle P \rangle_+)^2 - 4\langle P \rangle_- \langle P \rangle_+}}{\beta\langle P \rangle_- \langle P \rangle_+}. \quad (5.37)$$

The uncertainty on $A(E)$ from such an application of the polarization is determined via the usual error propagation,

$$\delta_P A(E) = \sqrt{\left(\frac{\partial A(E)}{\partial \langle P \rangle_+}\right)^2 (\delta \langle P \rangle_+)^2 + \left(\frac{\partial A(E)}{\partial \langle P \rangle_-}\right)^2 (\delta \langle P \rangle_-)^2}. \quad (5.38)$$

Although this method of determining the measured asymmetry is more rigorous than using a polarimetry value averaged over the two spin states, the effect on the asymmetry is small compared to the uncertainty from even the polarization alone, and inconsequential compared to the final uncertainty on the asymmetry.

5.2.5 Energy Reconstruction

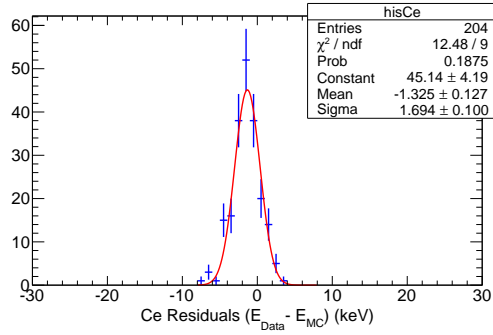
The energy enters the calculation of the asymmetry in the β term (speed of the electron) in equation 5.2.4.1, and thus it is essential to assess how well we can reconstruct the initial energy of an electron. The obvious choice for determining the efficacy of our energy calibration is to use the calibration peaks themselves and compare to Monte Carlo simulation. We apply the calibrations from chapter ?? to the data source peaks in all individual source runs, which maps the detector response to a reconstructed peak energy ($E_{\text{recon}}^{\text{data}}$), and then we apply our detector response model to the simulation peaks and extract a Monte Carlo reconstructed peak energy ($E_{\text{recon}}^{\text{MC}}$). We can then calculate a residual for every single run (and each conversion peak within that run) via $\text{Residual} = E_{\text{recon}}^{\text{data}} - E_{\text{recon}}^{\text{MC}}$. Upon collecting all of the residuals for each of the conversion electron peaks (Figures 5.9 and 5.10), we calculate ² the mean and sigma of the distributions, with values reported in table 5.5, and use them as the data points seen in figure 5.11. These points are a measure of the accuracy of the energy calibration at four discrete energies, the mean energies of the conversion electron lines themselves.

Table 5.5: Mean and σ of each conversion electron residual distribution as used in the energy uncertainty, figure 5.11.

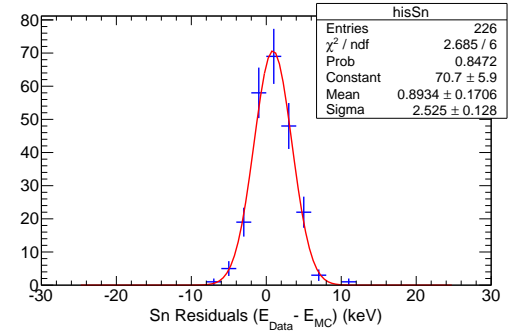
| | 2011-2012 | 2011-2012 |
|---------------------------|------------------------------|------------------------------|
| ^{137}Ce | $-1.43 \pm 1.81 \text{ keV}$ | $-0.80 \pm 2.00 \text{ keV}$ |
| ^{133}Sn | $0.91 \pm 2.52 \text{ keV}$ | $-2.24 \pm 2.87 \text{ keV}$ |
| ^{207}Bi (lower) | $-1.36 \pm 3.81 \text{ keV}$ | $-0.39 \pm 3.90 \text{ keV}$ |
| ^{207}Bi (upper) | $-1.55 \pm 5.77 \text{ keV}$ | $0.01 \pm 6.40 \text{ keV}$ |

The residuals at these discrete energies do not themselves tell us how well we do at intermediate energies. In the past, a conservative uncertainty envelope was drawn to encompass the calibration points [Men+13; Men14]. For the analysis presented here, a more quantitative determination of the uncertainty envelope was employed via methods developed by K. Hickerson for determination of limits on b_n from the previous UCNA spectrum ([Hic+17]). In short, the envelope is produced by sampling the coefficients of a quadratic, $f(E_{\text{recon}})$, from distributions that reproduce the residual data points seen in figure 5.11 with 1σ deviation. This obviously results in an asymmetric uncertainty band due to the asymmetric distribution of the data

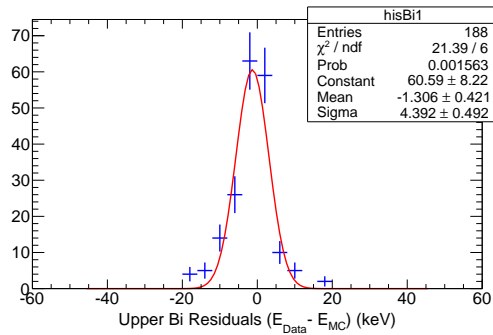
²The mean and sigma are calculated rather than fit so as to not neglect any non-gaussian tails in the distributions.



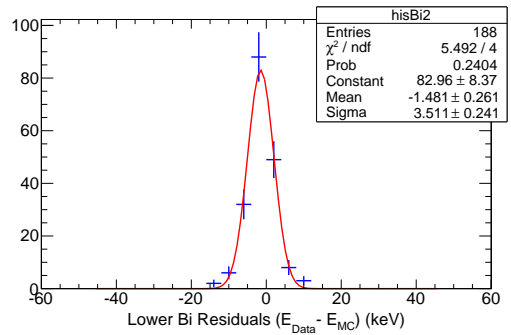
(a) Cerium Conversion Line



(b) Tin Conversion Line



(c) Lower Bismuth Conversion Line

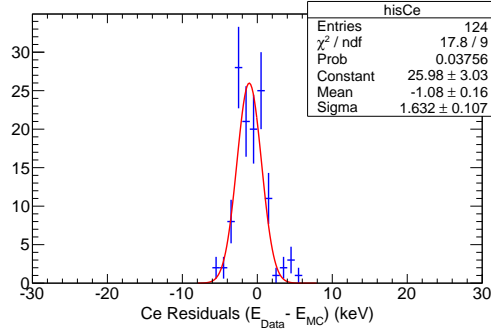


(d) Upper Bismuth Conversion Line

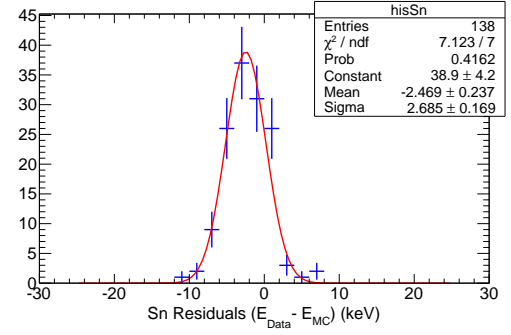
Figure 5.9: Distributions of the residuals for each conversion electron source line used in the 2011-2012 calibration. The mean and sigma reported in the fit box are not the same as those used in the energy uncertainty.

points about zero, but our conservative approach is to take the worst case uncertainty at every energy and use this as our symmetric final uncertainty. This produces the symmetric uncertainty band in figure 5.11.

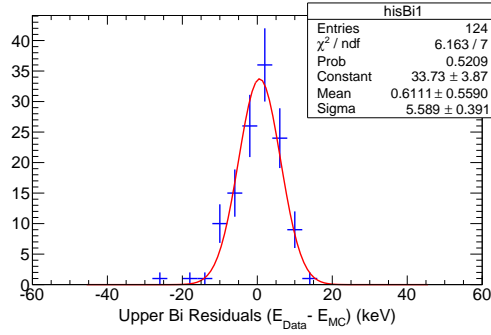
The symmetric worst case uncertainty band allows us to report a systematic uncertainty rather than a correction and an uncertainty from the energy reconstruction. The energy dependent uncertainty on A_0 for the maximal energy uncertainty (outer edge of the uncertainty envelope) is shown in figure 5.12. The uncertainty is then weighted by the data statistics in each bin to determine the total uncertainty in the final asymmetry, producing energy uncertainties of 0.17% and 0.25% for 2011-2012 and 2012-2013 respectively.



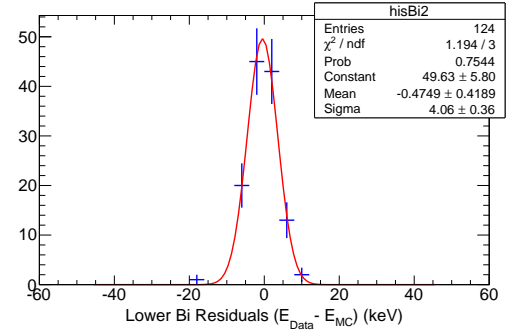
(a) Cerium Conversion Line



(b) Tin Conversion Line



(c) Lower Bismuth Conversion Line



(d) Upper Bismuth Conversion Line

Figure 5.10: Distributions of the residuals for each conversion electron source line used in the 2012-2013 calibration. The mean and sigma reported in the fit box are not the same as those used in the energy uncertainty.

5.2.6 Background Contributions

The raw measured spectra are highly contaminated with triggering events from something other than a neutron β -decay within the decay trap. Such unwanted events include ambient gamma ray events from neutron capture processes around the experimental hall, cosmic rays, and other unforeseen events which trigger the detector. Gamma ray events are highly suppressed due to the requirement of a coincidence trigger between the MWPC and the scintillator, and cosmic ray muon events are removed using a series of muon veto detection packages, which leaves the rest of the background to be subtracted using direct measurements of the electron spectrum in the absence of neutrons in the decay trap.

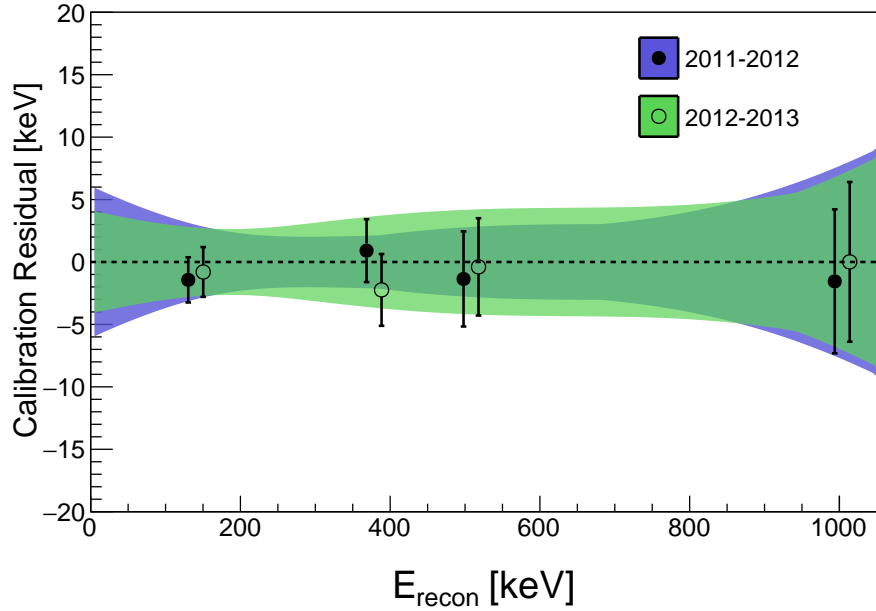


Figure 5.11: Plot of energy uncertainty vs. reconstructed energy. The points plotted are the mean and σ of all reconstructed calibration peaks of Ce, Sn, and the lower and upper Bi peaks in that order. The x-axis offset in the 2011-2012 and 2012-2013 points is artificial and only meant for visualization. The bands represent the energy uncertainty at any given electron energy for the two data sets.

5.2.6.1 Background Subtraction

Accompanying every β -decay run is a dedicated background run roughly 1/4 the length of the data taking run. The background events are processed in an identical manner to the data events and the rates are subtracted from the data rates. The uncertainties are propagated into the final rate, so in the absence of any non-statistical background fluctuations, the uncertainties from the backgrounds are inherently included in the extraction of the asymmetry. The background spectra for the different event types can be seen in figures 5.13 and 5.14.

The typical ratio between data and background rates is roughly 70:1 in 2011-2012 and 40:1 in 2012-2013, with the difference attributed to source performance issues. Figures 5.15 and 5.16 show the integrated rates in β -decay runs and background runs for the two geometries. The splitting in the β run rates is due to the difference between a spin-flipper “on” vs. spin-flipper “off” run, as the flipper “on” loading efficiency is approximately 66% that of a flipper “off” run.

The background subtraction transforms the rates in every bin in the following

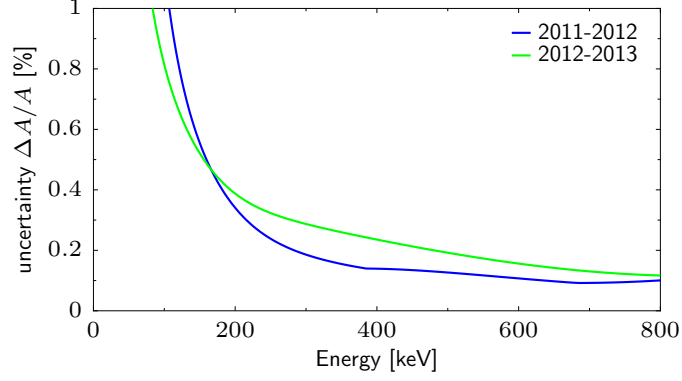


Figure 5.12: Plot of uncertainty on A_0 from the energy calibration vs. reconstructed energy for each of the 2011-2012 and 2012-2013 geometries. Weighting the energy dependent uncertainties shown here by the experimental statistics in each energy bin produces the final uncertainty on the extracted asymmetries.

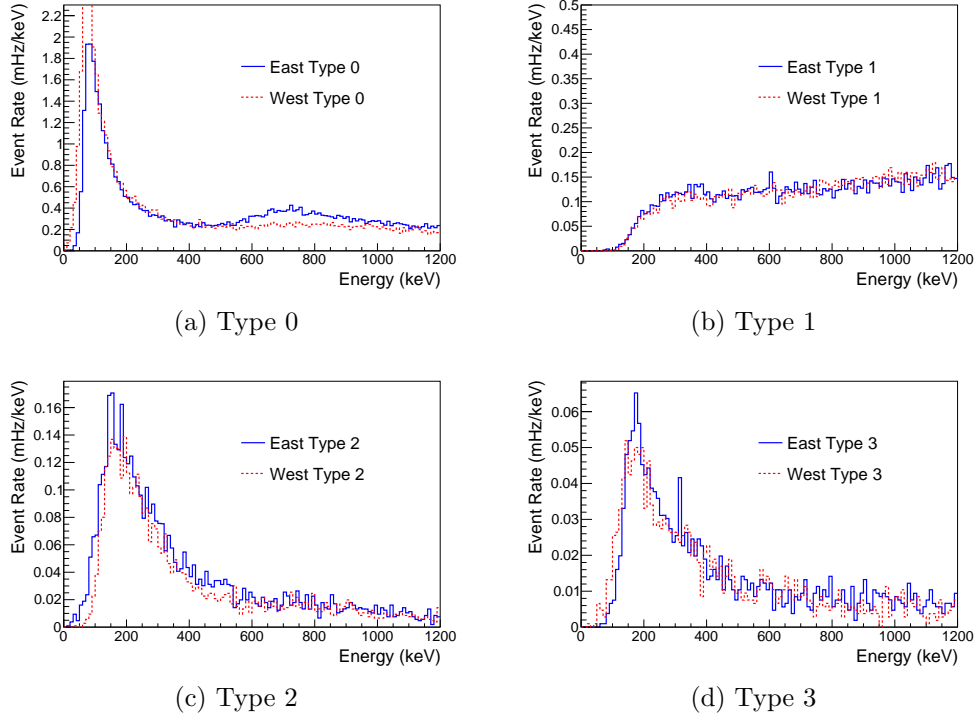


Figure 5.13: Total background spectra summed over all background runs for each event type in 2011-2012.

manner:

$$r_{\text{final},i} = \left(\frac{N_{\text{data},i}}{T_{\text{data}}} - \frac{N_{\text{bg},i}}{T_{\text{bg}}} \right) \pm \sqrt{\left(\frac{\sqrt{N_{\text{data},i}}}{T_{\text{data}}} \right)^2 + \left(\frac{\sqrt{N_{\text{bg},i}}}{T_{\text{bg}}} \right)^2} \quad (5.39)$$

where $r_{\text{final},i}$ is the background subtracted rate in bin i , N refers to counts, T is the

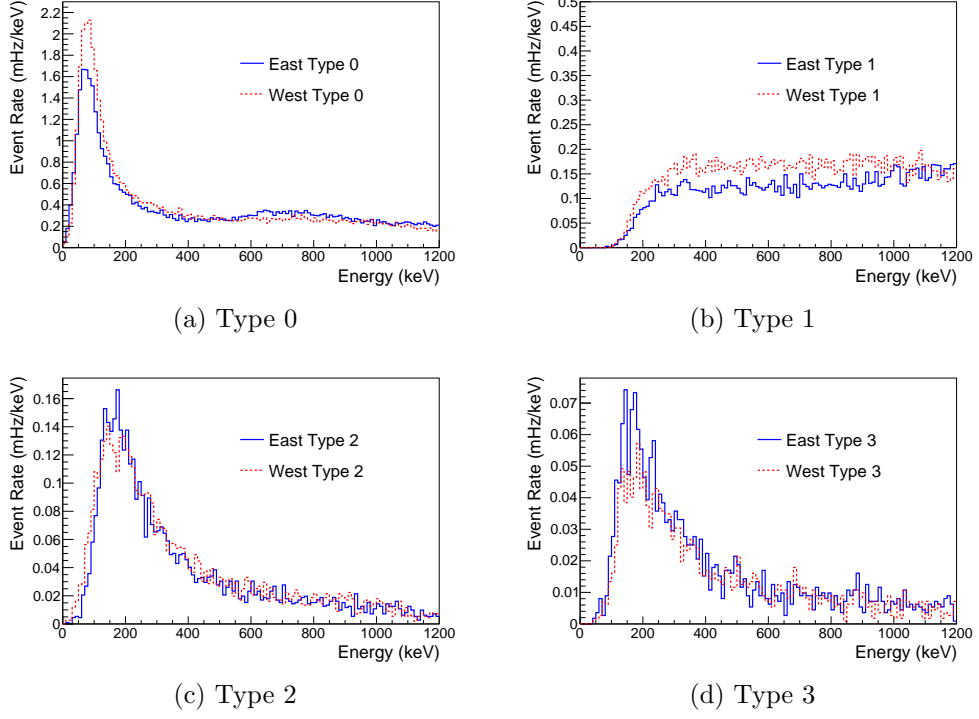
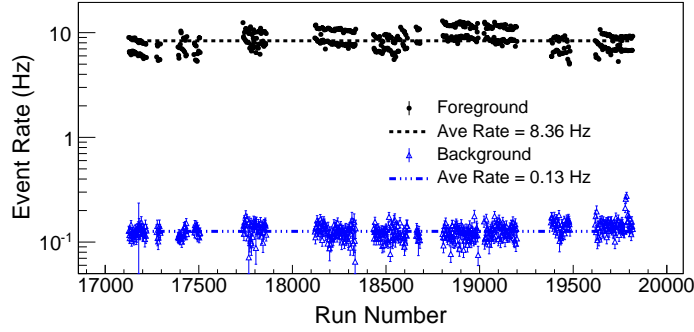


Figure 5.14: Total background spectra summed over all background runs for each event type in 2011-2012.

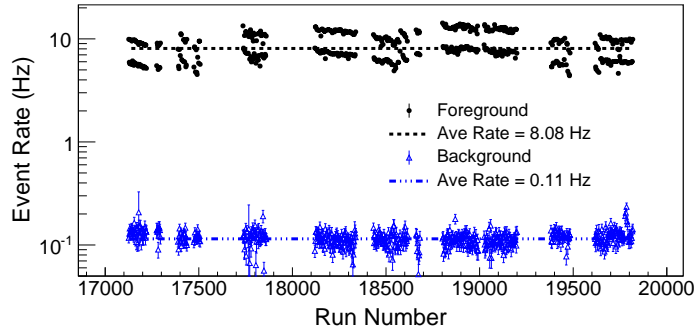
total time of a given run, and the subscript “data/bg” indicates whether the quantity comes from either the β -decay run or the background run. Equation 5.39 holds true as long as the counts in both the data and background run are large enough so that poisson statistics may be assumed. Below some count threshold ($N < 25$ for this analysis), we resort to an estimate of the uncertainty in a given bin. To do this, we utilize higher statistics reference spectra created by summing over all background runs for each spin state (\pm) and detector side (1,2) and applying the same data selection cuts (5.3.2.1) used for asymmetry analysis. The reference spectra are essentially combinations of those seen in figures 5.13 and 5.14. The expected background rate to be used in properly determining the background uncertainty is then determined by multiplying the reference background fraction in some energy bin by the total background counts in the background run, or

$$r_{\text{bg},i} = \frac{1}{T_{\text{bg}}} \left(N_{\text{bg},i} \pm \sqrt{N_{\text{bg,tot}} \frac{N_{\text{ref},i}}{N_{\text{ref,tot}}}} \right), \quad (5.40)$$

where subscript “ref” refers to the reference spectrum of background counts and subscript “tot” refers to the integrated total counts in the respective spectrum. This new background rate and uncertainty (note that only the uncertainty changes when



(a) East Side



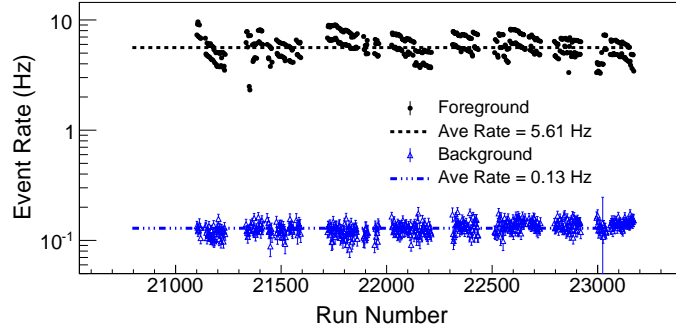
(b) West Side

Figure 5.15: Integrated event rates for 2011-2012 East and West sides. The splitting in the β run rates is due to the difference between a spin-flipper “on” vs. spin-flipper “off” run, as the flipper “on” loading efficiency is approximately 2/3 that of a flipper “off” run.

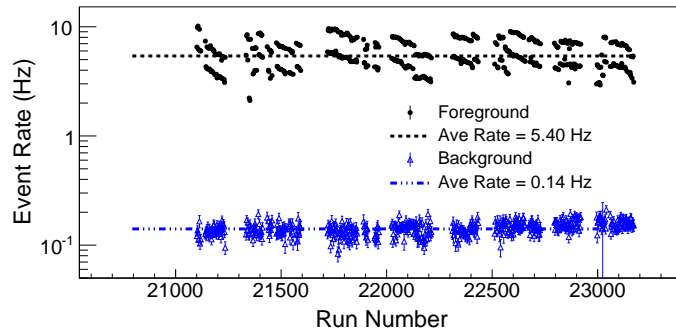
$N < 25$) are then used in equation 5.39. This method removes large statistical variation in the background uncertainties when the counts are low and gives an uncertainty to background rates that could be zero for a given bin.

5.2.6.2 Neutron Generated Backgrounds

Substantial work done previously by M. Mendenhall pioneered a thorough determination of the systematic correction to A_0 from neutron generated backgrounds, as can be found in [Men14]. Neutron generated backgrounds are not accounted for using normal background subtraction as the decay trap is void of neutrons during background runs. The correction comes mainly from UCN that escape the decay trap and interact with other components of the apparatus. The two main mechanisms studied were neutron capture on the aluminum wirechamber entrance and exit windows ($n + {}^{27}\text{Al} \rightarrow {}^{28}\text{Al}$) and on hydrogen in the scintillators ($n + {}^1\text{H} \rightarrow {}^2\text{H}$). These



(a) East Side



(b) West Side

Figure 5.16: Integrated event rates for 2012-2013 East and West sides. The splitting in the β run rates is due to the difference between a spin-flipper “on” vs. spin-flipper “off” run, as the flipper “on” loading efficiency is approximately 66% that of a flipper “off” run.

would create a small excess events in the background subtracted spectra above the β -decay endpoint, a common characteristic seen in both 2010 (used in [Men14]) and in the current analysis. Since the beyond endpoint rates agree within statistics and no changes were made to hardware outside the decay trap, adoption of the previously determined correction $\Delta A/A = 0.01(2)\%$ is assumed for this analysis.

5.2.6.3 Veto Efficiency Uncertainty

Gamma events and muon events that are vetoed by checking for coincidence between the scintillators and another component of the experiment could contribute an uncertainty to the asymmetry if the component used for determining coincidence behaves erratically. If all components are fairly stable in time, then even events which pass the veto due to inefficiency would be subtracted out using the typical background subtraction method mentioned above. To be conservative though, the uncertainty

from the previous analysis of $\pm 0.03\%$ was applied to the final asymmetry in case of any non-statistical fluctuations in the background rates.

5.2.7 Miscellaneous Systematic Corrections and Uncertainties

While the core Monte Carlo corrections described above make up the majority of the simulation motivated corrections from effects from the apparatus, there are several corrections and/or uncertainties determined from other Monte Carlo studies. These systematic effects are not determined on an energy dependent basis, but rather integrated over the final analysis window.

5.2.7.1 Wirechamber Efficiency

Since a dual trigger between the MWPC and the scintillator is required to differentiate between a background gamma ray and an electron (remember the MWPC is highly insensitive to gammas), electron events that fail to trigger the MWPC but trigger the scintillator will be misidentified as a gamma and will not be included in the asymmetry analysis. Higher energy, lower pitch angle events deposit less energy in the MWPC, thus these events suffer misidentification more often from MWPC efficiencies $< 100\%$. These same higher energy, lower pitch angle events contribute more to the raw asymmetry as seen by rewriting equation 5.2.4.1 and leaving the $\cos \theta$ dependence in,

$$A_{\text{SR}} = \langle P \rangle A(E) \beta \langle \cos \theta \rangle. \quad (5.41)$$

Missing these events effectively decreases the measured asymmetry, thus a systematic correction for such an effect should act to increase the magnitude of the measured asymmetry.

The goal for determining such a correction is to use simulated data to model the effect the efficiency of our MWPCs has on our measured asymmetry. First we need to determine the efficiency from data. A set of long ^{113}Sn runs with accompanying background runs were conducted at the end of the 2011-2012 run period. Using the background subtracted rates for MWPC triggering events (identified as an electron) and non-MWPC triggering events (identified as a gamma ray), one can set a lower limit on the wirechamber efficiency at the energy of the ^{113}Sn peak by calculating the ratio

$$\eta_{\text{MWPC}} = \frac{r_{\text{trigger}}}{r_{\text{trigger}} + r_{\text{NoTrigger}}}. \quad (5.42)$$

This is a lower limit because there could be contamination from actual gamma rays emitted by the ^{113}Sn source, but this contribution is quite small due to the gammas not being confined within the decay trap by the 1 T magnetic field and the small solid angle acceptance of the detectors for gammas originating at the center of the decay trap. The efficiencies found were $\eta_{\text{MWPC}} = 0.99912(40)$ and $\eta_{\text{MWPC}} = 0.99974(36)$ for the East and West detectors respectively.

The above efficiencies are only valid at the energy of the ^{113}Sn source, which is not ideal for use in the simulation as it stands. Instead, one would like to convert this into an energy deposition trigger threshold within the wirechamber. Using an MWPC energy threshold rather than an efficiency automatically creates an energy dependent efficiency, as the higher energy, lower pitch angle electrons will deposit less energy in the MWPC and will be less likely to trigger. Determining the threshold is done using simulations of the long ^{113}Sn runs. By scanning the MWPC threshold up from 0 keV, one can calculate the point at which the simulated wirechamber efficiency matches the wirechamber efficiency found using the data. The energy thresholds for the East and West MWPCs occur at roughly 0.969 keV and 0.874 keV respectively.

At this point, the integrated asymmetry is calculated for β -decay simulations with and without the MWPC efficiency in place, and then the correction is calculated in the usual way,

$$\Delta_{\text{MWPC}} = \frac{A_{\text{noThresh}}}{A_{\text{Thresh}}} - 1, \quad (5.43)$$

where the corrected asymmetry is that without the threshold since we want to remove the dependence on the MWPC efficiency. This was done for fifty independent batches of simulations, and the resulting fifty corrections were histogrammed and fit with a gaussian. The mean of this gaussian gives the correction, and the error on the mean gives the uncertainty. The final Δ_{MWPC} corrections are +0.13(1)% and +0.11(1)% for 2011-2012 and 2012-2013.

5.2.7.2 Gain Uncertainty

Gain corrections are applied on a run-by-run basis, so variations of the gain within each run will present themselves as an additional energy uncertainty. To study this effect, the individual endpoint values of every run from the data were histogrammed and the 1σ spread in the distribution was attributed to possible uncertainty in the gain during an individual run. The spread was taken to be ≈ 5 keV, which is a 0.0064% energy uncertainty at the endpoint. Assuming the same constant energy uncertainty across all electron energies and weighting by the experimentally observed

spectrum as was done in section 5.2.5, we find uncertainties of $\pm 0.16\%$ (2011-2012) and $\pm 0.17\%$ (2012-2013) from variations in PMT gain.

5.2.7.3 Magnetic Field Nonuniformity

As shown in section ??, the magnetic field is not uniform near the center of the decay trap, but rather has a dip surrounded by local maxima. Such conditions yield precarious scenarios for electrons with small longitudinal momentum (along the decay trap axis), as electrons with total momentum $p = \sqrt{p_{\parallel}^2 + p_{\perp}^2}$ in a magnetic field B_0 will be reflected if encountering a local maxima B_{\max} such that

$$B_{\max} > B_{\text{crit}} \equiv \left(\frac{p^2}{p_{\perp}^2}\right) B_0, \quad (5.44)$$

where B_{crit} is the critical condition for reflection. Thus a local field maximum will reflect a certain fraction of electrons, and a local field minimum, or field dip as we refer to it, will trap a certain fraction of electrons who originate within the dip.

The potential effect of nonuniform fields on the measured asymmetry is demonstrated quantitatively in appendix A. Qualitatively we understand the effect on the measured asymmetry using two ideal cases and considering the use of the super-ratio for extracting asymmetries. We also assume we have perfect detection efficiency in these cases.

The first nonuniformity we will consider is a central symmetric local maximum only. By central and symmetric I mean the field profile is identical on both sides of the maximum, which is at the center of the decay trap. A certain fraction of electrons both to the left and right of the maximum will be reflected back towards their initial location, changing the detected rates in each detector. Now spin state dependent and detector dependent acceptances nominally cancel in the super-ratio, but this modification to the rate is tied to the distribution itself, thus its effect is seen in the measured super-ratio asymmetry. This specific situation, in the context of appendix A, yields a dilution to the asymmetry that is dependent on the magnitude of the central maximum only.

The second scenario we will consider is that of a central symmetric field minimum (field dip). A field dip can trap β -decay electrons that originate in the lower field region if their longitudinal momentum is below some critical momentum, leaving them bouncing back and forth in the dip until they scatter off of the residual gas and gain enough momentum to escape. Such a scattering process randomizes the detected direction of the outgoing electron, thereby diluting the asymmetry.

Each ideal scenario alone produces a dilution to the asymmetry, and one would suspect that a correction to the asymmetry should be applied to increase the magnitude of the measured asymmetry, but simulation has shown the potential for nonuniform fields like those we measure to create an enhancement in the asymmetry. This very fact led to the calculation in appendix A, which shows that the position and shape of a field maximum or dip can create either enhancement or dilution to the asymmetry. This is not even considering that a field dip changes the angular distribution of the electrons it traps, which in turn changes the angular acceptance of the detected electrons, making electrons that never would have been detected before due to high pitch angle and low energy detectable by upscattering.

In conclusion, the intertwined dependence of the magnetic field correction on the shapes and positions of the nonuniformity and on the detector detection efficiencies prompted us to apply only an uncertainty from the field nonuniformity rather than a correction. Also, we only had reliable field data from 2011-2012, so a correction could not have been properly calculated for 2012-2013 without assumptions for the field profile. The uncertainty was determined by choosing a typical field profile and running fifty independent simulations with and without the field profile implemented for the 2011-2012 geometry. Both simulations were run with an increase in vacuum pressure from 10^{-5} Torr to 10^{-3} Torr in order to encourage upscattering from the field dip region, otherwise electron propagation time within the dip would have been far too computationally expensive. Since we are only studying the relative effect on the asymmetry, such a modification is acceptable. Upon histogramming the corrections to the asymmetry from the fifty independent simulations, one can extract the mean and error on the mean from a gaussian fit to the distribution, giving the mean correction to be applied of $-0.01(12)\%$, but as mentioned we will only apply an uncertainty and no correction, so for both geometries the uncertainty from the field nonuniformity is $\pm 0.12\%$.

5.3 Final Asymmetries

The last step in determining the asymmetry parameter is, of course, extracting the asymmetry from the β -decay data. Application of all described Monte Carlo corrections and uncertainties to the measured asymmetry produces a value for A_0 and thereby determines the ratio of the axial vector to vector coupling constants in the weak interaction, $\lambda \equiv \frac{g_A}{g_V}$.

The general process includes choosing the proper subset of our data for the asym-

metry extraction, making analysis cuts, optimizing our final analysis energy window to minimize uncertainties, and finally unveiling the result. This section is dedicated to these steps.

5.3.1 Blinding

All of the analysis discussed up until this point, and even all stages of the asymmetry extraction up until revealing the final result, are completed using blinded data, making this entire analysis a blind analysis. The idea behind blind analyses is to introduce a bias to your data in some way that would not allow anyone to know the final answer during all systematic studies. This removes the human temptation to skew corrections in such a way that the new result converges towards a personally desired result. This could be an attempt to achieve agreement with previous results or to move further from a null hypothesis to achieve discovery. Either way, avoiding this temptation makes for better science.

For this analysis, blinding was achieved by modifying the time stamps of every event in such a way that the the blinding factor (as part of the detector rates) would not cancel in the super-ratio. This required altered time stamps which are spin-state and detector dependent and do not cancel in the super-ratio. We produce two independent random blinding factors, $f_{1,2}$, such that

$$t_{1,2}^{\pm} = (1 \pm f_{1,2}) \cdot t \quad (5.45)$$

where t is the global time and $t_{1,2}^{\pm}$ are the blinded times for each detector in each spin state. We completed detector calibrations, all systematic corrections, and the polarimetry analysis prior to unblinding, at which point all rates were recalculated using the proper global time t , generating the final unblinded asymmetries.

5.3.2 Data Selection and Processing

The data selection step generally involves choosing events that are “good” electron events, trying to preserve as many as possible to increase statistical power while avoiding unforeseen systematic effects from questionable events. These cuts are also applied to the simulated data when determining systematic corrections for consistency. Thus, if the model appropriately accounts for all experimentally induced deviations from the ideal asymmetry, the asymmetries from data and Monte Carlo should be consistent.

5.3.2.1 Cuts

The first cut applied is a fiducial cut selecting events within 50 mm of the center of the decay trap. The fiducial cut removes events that could have potentially interacted with the decay trap wall, as the maximum radius of the electron's spiral around the magnetic field is 7.76 mm and the wall of the decay trap is 62.2 mm from the center. Interactions with the walls of the decay trap can modify the energy and direction of the electron, thereby affecting the measured asymmetry. While the Monte Carlo model should be able to correct for this, avoiding the interactions altogether is advantageous.

We also remove from data and background runs any events that occur when the proton beam is dropped, which means no neutrons are being loaded into the trap. Since we use the rate over an entire run in the super-ratio, using time periods with few events reduces the average rate. The real issue with this comes from the background subtraction, which is meant to account for backgrounds that could stem from beam related interactions. If either the β -decay or background run has a highly disproportionate amount of run time with the proton beam missing, the background subtraction for that run is not as effective. A running monitor of the UCN production is used to determine when to cut intervals of data, dropping the events when the UCN rate in UCN Monitor 1 (the first monitor beyond the UCN source) falls below 2 Hz. The rate for all data was generally > 20 Hz. Any events that occur within 0.05 s of the proton beam burst are also cut to improve the signal to background ratio.

Two wirechamber cuts, beyond the position cut, were also applied. The first is a cut on the shape of the wirechamber signal, based on an algorithm developed by a collaborator C. Swank from Caltech. While the algorithm classifies events as one of eight shapes based on the magnitude of the signal on each wire group, the cut was used to remove non-physical shapes like multiple positions in one wirechamber. The second wirechamber cut simply checks that at least one cathode wire group in each plane was above threshold so that a position can be assigned to that event. Since a model of the cathode response was developed for the Monte Carlo in this analysis, these same cuts could be applied to the simulation to account for any systematic effect if these events are not simply random.

The last cut applied is an energy cut where we check that each event lies within the energy range $190 \text{ keV} < E_e < 740 \text{ keV}$. Within this energy range, the events are further separated into 10 keV energy bins for energy dependent asymmetry extraction. The determination of this analysis energy window is described below in section 5.3.3.2. All asymmetries shown from now on will be fit or integrated over this energy range.

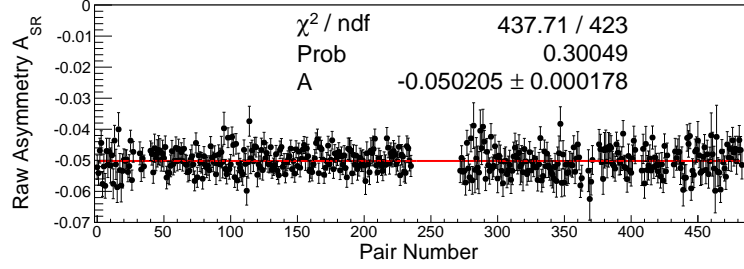
5.3.2.2 Data Taking Structure

For use of the super-ratio technique, one must use at least two runs with differing loaded neutron spin states. For the UCNA experiment, we utilize what we call an octet data structure, consisting of eight β -decay runs, eight background runs, and eight depolarization runs, with the spin-state changing in such a way that produces four runs from each \pm spin state. The details of this method can be found in [Pla+12]. This method allows for construction of three different super-ratio asymmetries: octet asymmetries (utilizing all eight background subtracted β -decay runs in the asymmetry), quartet asymmetries (using four consecutive spin-flipped runs in the asymmetry), and pair asymmetries (using two consecutive spin-flipped runs). Each octet can potentially produce four pair asymmetries and two quartet asymmetries. We use the octet asymmetries in the extraction of the final asymmetry, as this structure lends to more efficient cancellation of time varying backgrounds. Figure 5.17 shows the raw asymmetries extracted from all three types of data groups. The results are consistent within statistical uncertainties, and the χ^2/NDF indicates the fluctuations are statistical.

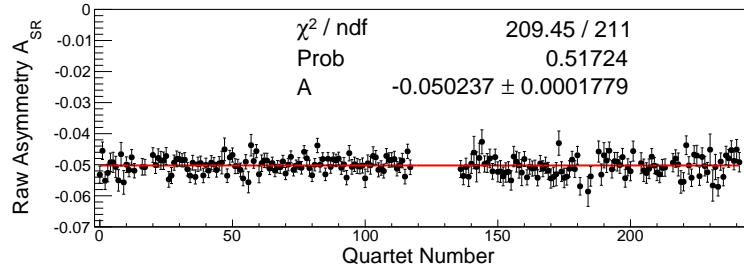
5.3.2.3 Analysis Choices

We have identified four detected electron event types thus far in this analysis, namely Type 0, 1, 2, and 3. In summary, Type 0 events are those which are identified as single detector events, meaning they trigger one detector package only, and they make up almost 95% of detected events. Types 1, 2, and 3 are identified as backscattering events, with Type 1 events triggering both scintillators, while 2 and 3 trigger both wirechambers but only one scintillator. Based on solely trigger logic, a Type 2 cannot be distinguished from a Type 3, but a delineation can be made between them given their energy deposition in the MWPC. See section ?? for a detailed description of the backscattering events and the MWPC calibration used to separate them.

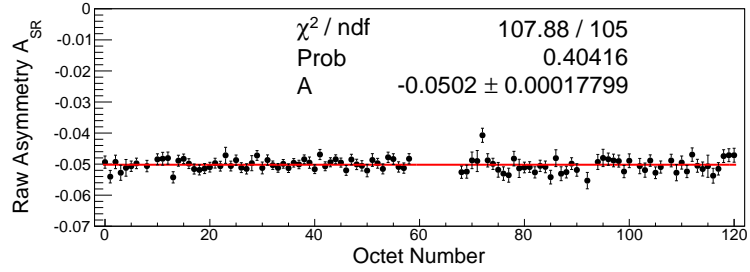
Inclusion of any subset of the aforementioned event types in the analysis produces different asymmetries, where any choices that have like event types are correlated at the level of the fractional statistical uncertainty of the like types. One may also decide to include the Type 2/3 events as unseparated or separated by the MWPC energy cut, giving yet another set of analysis choices. For this analysis, we used all event types with the Type 2 and Type 3 separated. This choice utilizes maximal statistics, while separating the Type 2/3 events requires smaller systematic corrections and uncertainties than leaving them unseparated.



(a) Pair Asymmetries

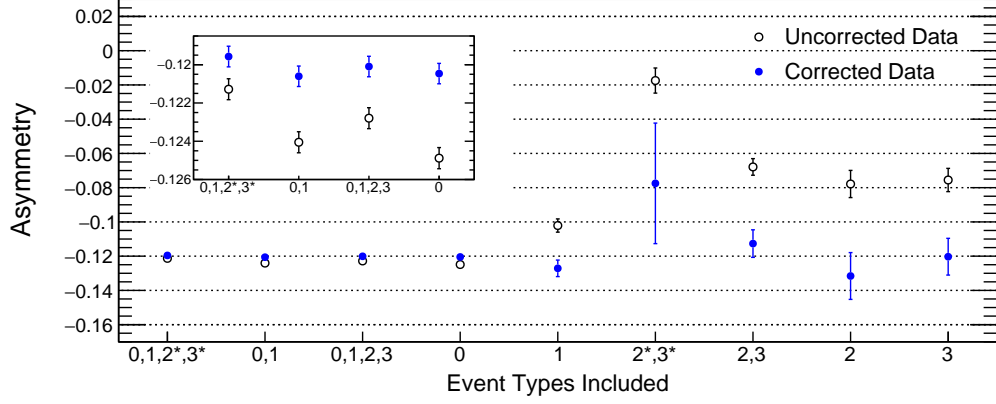


(b) Quartet Asymmetries

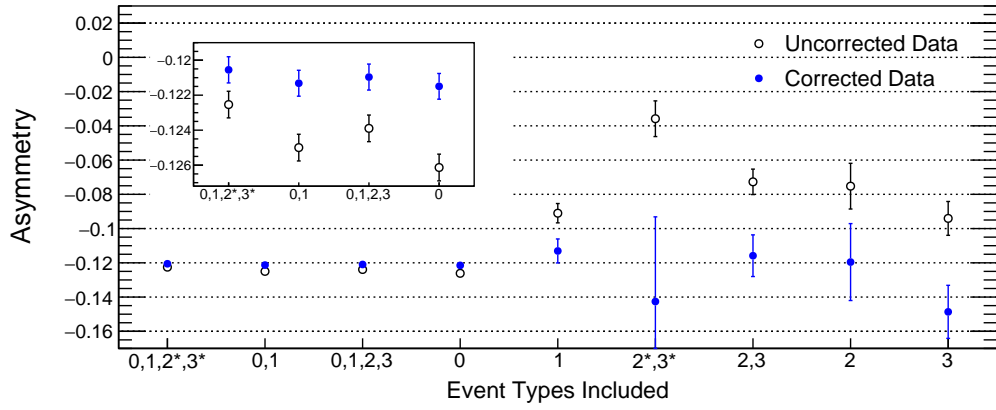


(c) Octet Asymmetries

Figure 5.17: All raw super-ratio asymmetries as a function of group number, whether octet, quartet, or pair. There are no systematic corrections applied, and the asymmetries are integrated over the analysis window 190-740 keV. The split in the data is a batch of data from 2012-2013 that had to be discarded due to bad timing information.



(a) 2011-2012



(b) 2012-2013

Figure 5.18: Asymmetries for different subsets of data. The * signifies unseparated Type 2 and Type 3 events. The inset shows the asymmetries that include Type 0 events, as the uncertainties are too small to see in the main figure. The only corrections applied to these asymmetries are the energy dependent Monte Carlo corrections and the polarization correction. The error bars are purely statistical, so the observed agreement between asymmetries is a lower limit.

Figure 5.18 shows the asymmetries for all analysis choices considered, with the event types included in the asymmetry extraction listed on the horizontal axis. There is a noticeable improvement in the agreement across all analysis choices compared to previous analyses, indicating improvement in the Monte Carlo corrections, namely Δ_2 and Δ_3 . The uncertainties in the figure are purely statistical, so the agreement seen is a worst case scenario as inclusion of systematic uncertainties inflates the error bars.

5.3.3 Determining A_0

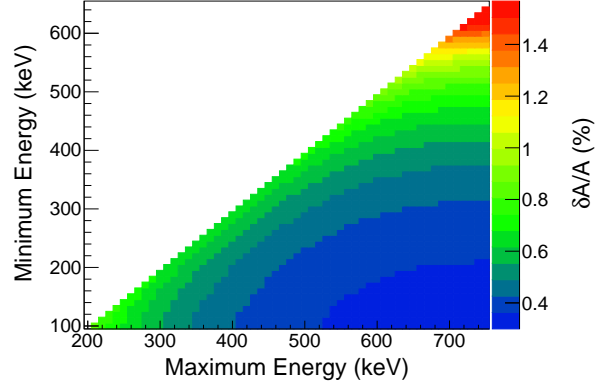
5.3.3.1 Combining Results

After selecting the data to be used in the final determination of the asymmetry, one is left with two separate blinded results, one from each geometry (2011-2012 and 2012-2013). The results are then combined via a method developed for the previous analysis by M. Mendenhall [Men14]. In summary, the combination is a modified weighted average that takes into account correlations between all uncertainties. Uncorrelated uncertainties will improve the final uncertainty, while correlated uncertainties cannot. The method inherently solves for the weighting factors that minimize the total uncertainty of the combined final result.

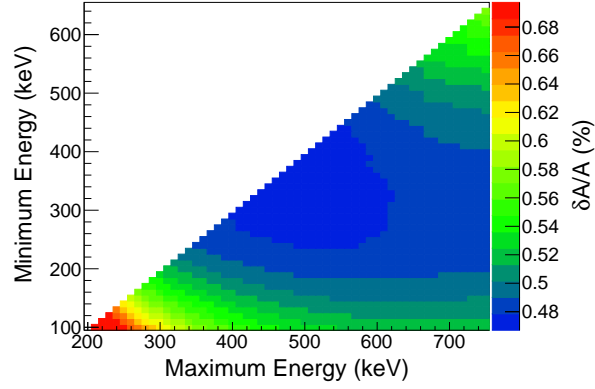
For this analysis, the individual systematic uncertainties from each geometry (i.e. Δ_2 from 2011-2012 and 2012-2013) are taken to be completely correlated, but they are uncorrelated with all other uncertainties. The statistical uncertainty of one geometry is the only uncertainty treated as uncorrelated with its counterpart from the other geometry, as we would like to take advantage of the combined statistical power of each result.

5.3.3.2 Optimization of energy range

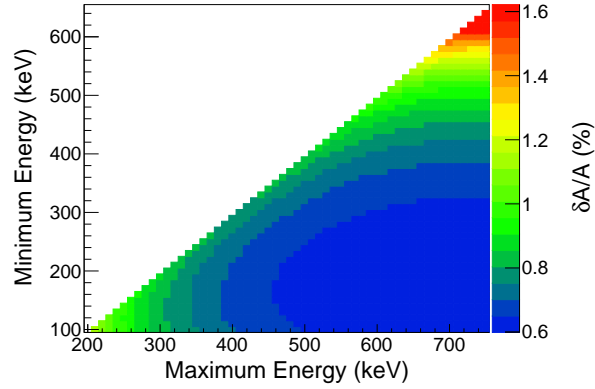
Once the framework for combining results is in place, the energy analysis window must be determined. Ideally, the analysis window should be one that minimizes the total uncertainty given the subset of data chosen for the final result, but, because several of the integrated corrections require the analysis window as input, we only consider the uncertainties from statistics, energy reconstruction, and energy dependent Monte Carlo corrections during minimization.



(a) Statistical Uncertainty



(b) Systematic Uncertainty (Combined Energy Uncertainty and Monte Carlo uncertainty)



(c) Combined systematic and statistical uncertainty

Figure 5.19: Plots of the fractional uncertainty on the extracted asymmetry for given minimum and maximum limits on the analysis window. The minimum of the combined systematic and statistical uncertainty is used for the final analysis window, $190 \text{ keV} < E_e < 740 \text{ keV}$.

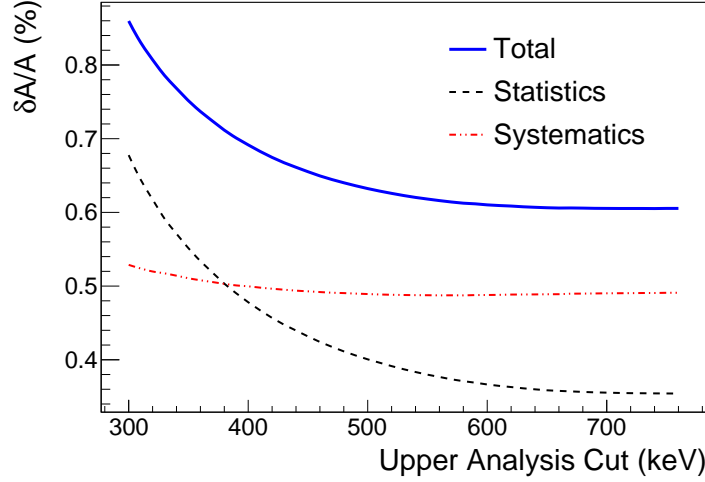


Figure 5.20: Statistical and systematic errors used in minimization of the energy window. This is a projection of figure 5.19 about the minimum window cut of 190 keV to show the dependence on energy cut more effectively.

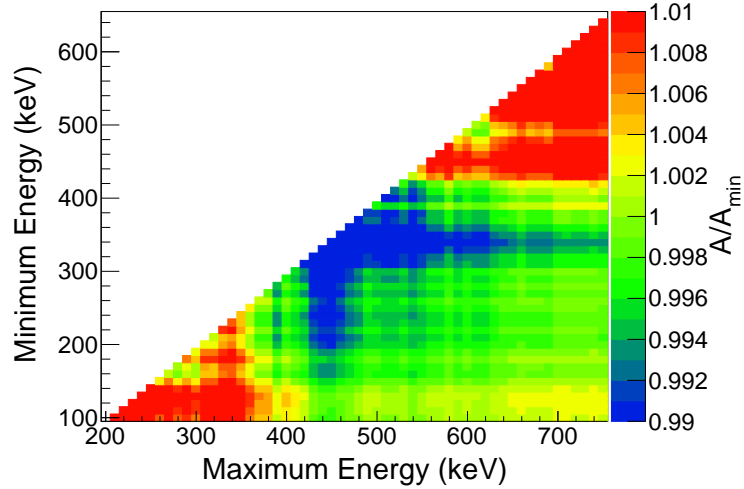


Figure 5.21: Ratio of the asymmetry for every possible energy window divided by the asymmetry of the window with the minimum uncertainty. The closer to the lower right hand corner, the larger the analysis window. We see that there is a region of highly consistent asymmetries covering the bottom right hand corner, which is where our analysis window of choice lies. When comparing to figure 5.19, we also see that, given the uncertainties for every analysis window, nearly all asymmetries are consistent within error.

The final energy window is calculated by scanning all possible energy windows in 10 keV increments, with a minimum lower bound at > 100 keV and a maximum upper bound of < 780 keV. The total width of the energy window is set to start at 100 keV to

save on computation time but is not limited beyond that. Upon exploring all energy windows, the minimum combined uncertainty occurs at $190 \text{ keV} < E_e < 740 \text{ keV}$ shown. Figure 5.19 shows the uncertainty contributions as a function of energy window. The final plot shows the combined uncertainty from all three contributions, and we see that the window $190 \text{ keV} < E_e < 740 \text{ keV}$ falls within the area of the minimum uncertainty. Once we choose the minimum edge of our window, we can view the dependence of the final uncertainty as a function of the upper edge of the analysis window as seen in figure 5.20. Here we see the total uncertainty becomes essentially constant beyond an upper window cut of 690 keV. The dependence of the asymmetry on energy window can be seen in figure 5.21. The asymmetry is stable within $\pm 0.3\%$ upon changing the analysis window by roughly 100 keV in either direction about the minimum window, as evidenced by the uniform area in the lower right hand corner of the plot. Thus the asymmetry is fairly stable among reasonable choices for the analysis window. Even in regions of figure 5.21 where the asymmetry appears to change noticeably, when taking into account the uncertainty for that asymmetry as plotted in 5.19, one sees that the majority of asymmetries remain consistent.

5.3.3.3 Unblinded Result

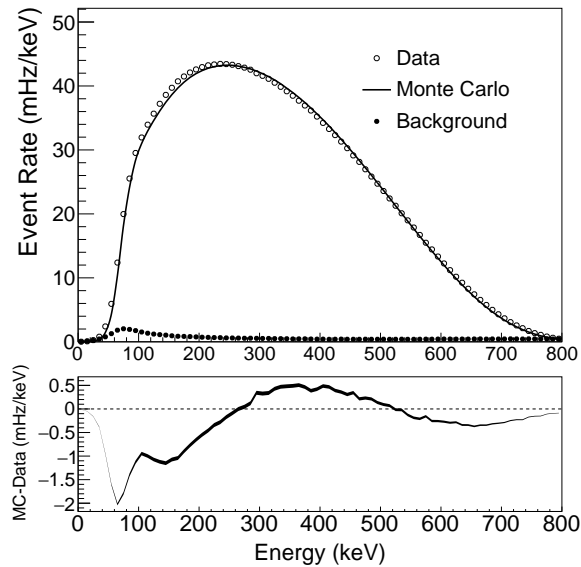


Figure 5.22: Final beta decay spectrum from data (open circles), Monte Carlo (solid line), and the subtracted background (closed circles). The bottom shows the difference between the Monte Carlo spectrum and the data.

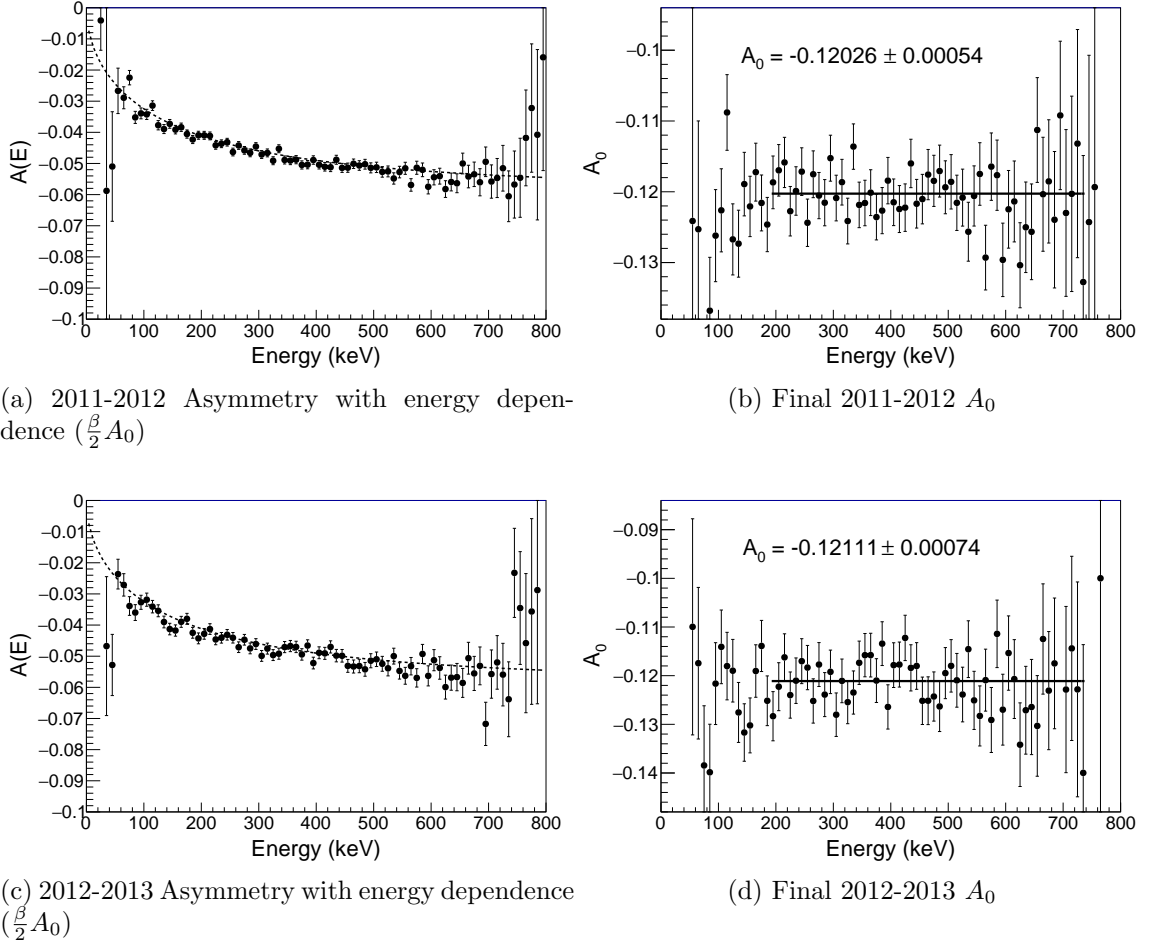


Figure 5.23: Final unblinded 2011-2012 and 2012-2013 asymmetry with all systematic corrections applied. The dashed line in a.) and c.) uses PDG $A_0 = -0.1184$ for comparison. The fits in b.) and d.) are over the final analysis window, $190 \text{ keV} < E_e < 740 \text{ keV}$. The uncertainties are statistical only.

On August 16, 2017, upon completion of all systematic studies and the asymmetry analysis code, the data was unblinded and the asymmetries recalculated using the proper time stamps. The energy dependent asymmetries and final asymmetries for the two geometries, 2011-2012 and 2012-2013, are shown in figure 5.23, with fits over the final analysis window of $190 \text{ keV} < E_e < 740 \text{ keV}$. The unblinded asymmetries with both statistical and systematic uncertainties accounted for are $A_0 = -0.12026(54)_{\text{stat}}(67)_{\text{syst}}$ and $A_0 = -0.12111(74)_{\text{stat}}(69)_{\text{syst}}$ for 2011-2012 and 2012-2013 respectively. Utilizing the method described in section 5.3.3.1 for combining results, the 2011-2012 and 2012-2013 asymmetries were combined with weights of 0.67 (2011-2012) and 0.33 (2012-2013), yielding a final value of $A_0 = -0.12054(44)_{\text{stat}}(68)_{\text{syst}}$ corresponding to a value for the ratio of the axial-

vector to vector coupling constants of $\lambda \equiv \frac{g_A}{g_V} = -1.2783(22)$, where the statistical and systematic uncertainties have been added in quadrature.

We also report a combined result using our previous measurement [Men+13] and a similar weighting method as above, only now we set all systematic uncertainties to the smallest reported value between the two measurements and treat them as completely correlated. This in turn means we do not benefit beyond the best measurement of any systematic uncertainty, but that we take advantage of the increased statistics. This culminates in the combined UCNA results of $A_0 = -0.12015(34)_{\text{stat}}(63)_{\text{syst}}$ and $\lambda \equiv \frac{g_A}{g_V} = -1.2772(20)$, with weights of 0.39 for the previous result [Men+13] and 0.61 for the result from this analysis.

5.4 Future Outlook for UCNA and A_0 Measurements

While this measurement concludes results for A_0 from the UCNA experiment in its current capacity, there are hopes for a next generation UCNA+ experiment. The limitations of the current experiment, namely the backscattering, $\cos \theta$, and energy reconstruction uncertainties, prevent UCNA from achieving future competitive results of much more precision than that reported above.

With this in mind, UCNA+ intends to take actions to drastically reduce Δ_3 , or the $\cos \theta$ correction, which can be achieved by decreasing the fraction of electrons that are lost due to inefficiencies within the spectrometer. These mainly come from the existence of the foils at the end of the decay trap, so the idea is to remove the foils and no longer confine the neutrons within the decay volume. With the recent upgrades in the UCN source performance, trapping the neutrons within the decay volume is less important than it was during previous UCNA runs. Another interesting proposal is to have annular endcaps with a hole in the middle. This would allow one to make a radial position cut on the electron events to use events which either originated in the region with effectively no endcap or in the outer region where the electron would see an endcap. Comparisons between these two types of events sheds light on the behavior of the correction from data itself, and when compared to Monte Carlo can help determine the level at which the Monte Carlo corrections are accurate. This comparison with Monte Carlo may improve both the backscattering and $\cos \theta$ systematic uncertainties.

As for the energy reconstruction, detectors with better linearity and perhaps a

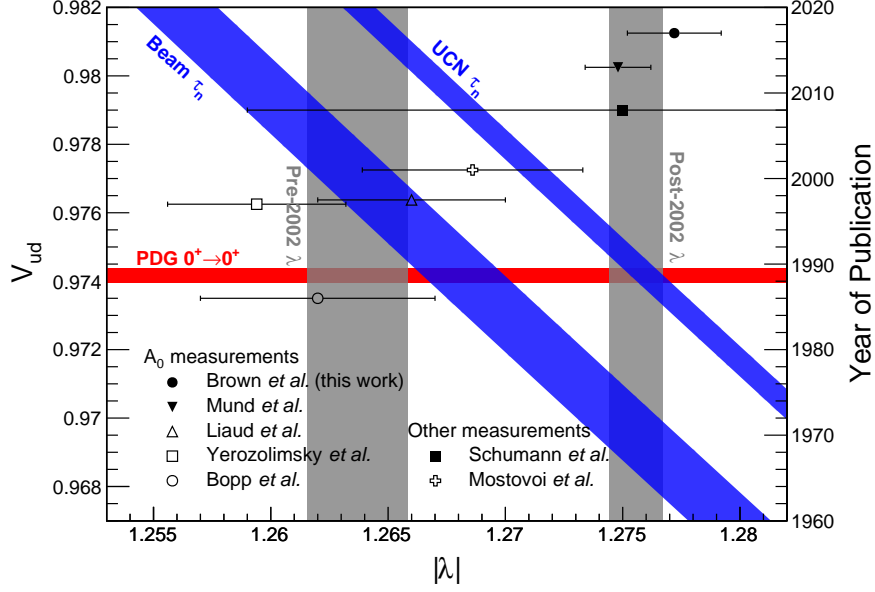


Figure 5.24: Status of V_{ud} , the neutron lifetime, and λ measurements. The λ result bands (vertical) are divided into pre-2002 [Bop+86; Yer+97; Lia+97] and post-2002 [Mos+01; Sch+08; Mun+13; Men+13] results, where the distinction is made using the date of the most recent result from each experiment. The right axis shows publication year for the individual lambda measurements included in the calculation of the λ bands (closed markers for post-2002, open markers for pre-2002). Note that the result of this work (Brown *et al.*) is the combined UCNA result from [Men+13] and the current analysis, and the Mund *et al.* result is the combined PERKEOII result from [Abe+02; Mun+13]. The diagonal bands are derived from neutron lifetime measurements and are separated into neutron beam [Yue+13; Byr+96] and UCN bottle experiments, which consist of material bottle storage [Ser+05; Arz+15; Ste+12; Pic+10; Mam+93] and magnetic bottle storage [PJ+17]. The V_{ud} band (horizontal) comes from superallowed $0^+ \rightarrow 0^+$ nuclear β -decay measurements [PG+16]. The error bands include scale factors as prescribed by the Particle Data Group [PG+16].

self-position-reconstructing scintillator would be useful. With position reconstruction accomplished within the scintillator, the wirechambers could be removed thus reducing the $\cos \theta$ correction further. Another potential improvement, although admittedly difficult, would be the development of a calibration method which samples the entire fiducial volume, or at least a larger fraction of the detector face. The activated Xenon spectrum highlights the promise of such a method, as it fills the entire spectrometer during position map calibration runs, but the existence of discrete conversion lines within the calibration gas would create a completely determined calibration for every “pixel” of the detector. This would remove the need for position maps altogether and would avoid any potential bias from measuring the position dependence of the

detector with a characteristic of the Xenon spectrum that is beyond the endpoint of the electron spectrum, an imperfect method when the detector shows any non-linear behavior.

The future of A_0 and λ measurements is quite promising given the status of recent results. Figure 5.24 illustrates the current dilemma facing the experimental nuclear physics community regarding weak interactions and the neutron itself. Of measurements included in the current 2017 Particle Data Group (PDG) average, there is a several σ discrepancy between λ measurements prior to 2002 and those after 2002. One also sees from the figure that a similar splitting of neutron lifetime values has occurred, with the difference seemingly arising between experiments using neutron beams [Yue+13; Byr+96] and those using UCN (both material bottle [Ser+05; Arz+15; Ste+12; Pic+10; Mam+93] and magnetic bottle [PJ+17] measurements). When combined with measurements of the CKM matrix element V_{ud} from super-allowed $0^+ \rightarrow 0^+$ nuclear β -decays, a clearly favorable scenario presents itself, and further precision measurements of both λ and τ_n will assist in settling the matter.

The older pre-2002 measurements of λ prompt the PDG to apply a scale factor of 2.2 to the uncertainty on the global average for λ (and a scale factor of 2.4 to A_0). The PDG only includes in the calculation of the scale factor those measurements that satisfy

$$\delta x_i < 3\sqrt{N}\delta\bar{x}, \quad (5.46)$$

where x_i refers to one measurement of quantity x out of N measurements and $\delta\bar{x}$ is the non-scaled error on the weighted average \bar{x} [PG+16]. So while the older measurements carry very little weight in the average value and the non-scaled uncertainty, they drastically affect the χ^2 . One solution to this issue is to improve the uncertainty on modern A_0 and λ measurements, as inclusion of a 0.1% result for A_0 (yielding a 0.025% result for λ), removes the pre-2002 results for λ from those that enter the calculation of the scale factor. Current results from PERKEOII are already $< 0.3\%$ on A_0 , and hopefully a next generation UCNA+ experiment can contribute the desired precision to remove the scale factor from the PDG average values for A_0 and λ altogether.

Copyright© Michael A-P Brown, 2017.

Appendix A

Magnetic Field Non-Uniformity and the Super-Ratio

Copyright© Michael A-P Brown, 2017.

References

- [Abe+02] Hartmut Abele et al. “Is the unitarity of the quark-mixing CKM matrix violated in neutron β -decay?” In: *Physical Review Letters* 88.21 (2002), p. 211801.
- [Arz+15] S Arzumanov et al. “A measurement of the neutron lifetime using the method of storage of ultracold neutrons and detection of inelastically up-scattered neutrons”. In: *Physics Letters B* 745 (2015), pp. 79–89.
- [Bil+60] SM Bilenkii et al. “On the theory of neutron beta-decay”. In: *SOVIET PHYSICS JETP-USSR* 10.6 (1960), pp. 1241–1244.
- [Bop+86] Peter Bopp et al. “Beta-Decay Asymmetry of the Neutron and g_A/g_V ”. In: *Physical Review Letters* 56.9 (1986), p. 919.
- [Byr+96] J Byrne et al. “A revised value for the neutron lifetime measured using a Penning trap”. In: *EPL (Europhysics Letters)* 33.3 (1996), p. 187.
- [Cas09] Diego Casadei. “Efficiency measurement: a Bayesian approach”. In: *ArXiv e-prints* (2009).
- [GZ01] Susan Gardner and Chi Zhang. “Sharpening low-energy, standard-model tests via correlation coefficients in neutron β decay”. In: *Physical review letters* 86.25 (2001), p. 5666.
- [Hic+17] KP Hickerson et al. “First direct constraints on Fierz interference in free-neutron β decay”. In: *Physical Review C* 96.4 (2017), p. 042501.
- [JTWJ57] JD Jackson, SB Treiman, and HW Wyld Jr. “Possible tests of time reversal invariance in beta decay”. In: *Physical Review* 106.3 (1957), p. 517.
- [Lia+97] P Liaud et al. “The measurement of the beta asymmetry in the decay of polarized neutrons”. In: *Nuclear Physics A* 612.1 (1997), pp. 53–81.

- [Mam+93] W Mampe et al. “Measuring neutron lifetime by storing ultracold neutrons and detecting inelastically scattered neutrons”. In: *JETP LETTERS C/C OF PIS’MA V ZHURNAL EKSPERIMENTAL’NOI TEORETICHESKOI FIZIKI* 57 (1993), pp. 82–82.
- [Men+13] MP Mendenhall et al. “Precision measurement of the neutron β -decay asymmetry”. In: *Physical Review C* 87.3 (2013), p. 032501.
- [Men14] Michael Praetorius Mendenhall. “Measurement of the neutron beta decay asymmetry using ultracold neutrons”. PhD thesis. California Institute of Technology, 2014.
- [Mos+01] Yu A Mostovoi et al. “Experimental value of GA/GV from a measurement of both P-odd correlations in free-neutron decay”. In: *Physics of Atomic Nuclei* 64.11 (2001), pp. 1955–1960.
- [Mun+13] D Mund et al. “Determination of the Weak Axial Vector Coupling $\lambda = g_A/g_V$ from a Measurement of the β -Asymmetry Parameter A in Neutron Beta Decay”. In: *Physical review letters* 110.17 (2013), p. 172502.
- [PG+16] C Patrignani, Particle Data Group, et al. “Review of particle physics”. In: *Chinese physics C* 40.10 (2016), p. 100001.
- [Pic+10] A Pichlmaier et al. “Neutron lifetime measurement with the UCN trap-in-trap MAMBO II”. In: *Physics Letters B* 693.3 (2010), pp. 221–226.
- [PJ+17] RW Pattie Jr et al. “Measurement of the neutron lifetime using an asymmetric magneto-gravitational trap and in situ detection”. In: *arXiv preprint arXiv:1707.01817* (2017).
- [Pla+12] Bg Plaster et al. “Measurement of the neutron β -asymmetry parameter A 0 with ultracold neutrons”. In: *Physical Review C* 86.5 (2012), p. 055501.
- [Sch+08] Marc Schumann et al. “Measurement of the proton asymmetry parameter in neutron beta decay”. In: *Physical review letters* 100.15 (2008), p. 151801.
- [Ser+05] A Serebrov et al. “Measurement of the neutron lifetime using a gravitational trap and a low-temperature Fomblin coating”. In: *Physics Letters B* 605.1 (2005), pp. 72–78.
- [Sir67] A Sirlin. “General properties of the electromagnetic corrections to the beta decay of a physical nucleon”. In: *Physical Review* 164.5 (1967), p. 1767.

- [Ste+12] Albert Steyerl et al. “Quasielastic scattering in the interaction of ultracold neutrons with a liquid wall and application in a reanalysis of the Mambo I neutron-lifetime experiment”. In: *Physical Review C* 85.6 (2012), p. 065503.
- [Wil82] Denys H Wilkinson. “Analysis of neutron β -decay”. In: *Nuclear Physics A* 377.2-3 (1982), pp. 474–504.
- [Yer+97] B Yerozolimsky et al. “Corrigendum: Corrected value of the beta-emission asymmetry in the decay of polarized neutrons measured in 1990”. In: *Physics Letters B* 412.3-4 (1997), pp. 240–241.
- [You17] A. R. Young. “Super-ratio with explicit spin-up and spin-down polarizations”. In: *Private Communication* (2017).
- [Yue+13] AT Yue et al. “Improved determination of the neutron lifetime”. In: *Physical review letters* 111.22 (2013), p. 222501.

Vita

A brief vita goes here.